Microphysical characterisation of West African MCS anvils

Dominique Bouniol, Julien Delanoë, Christophe Duroure, Alain Protat, Vincent Giraud, Guillaume Penide

Microphysical characterisation of West African MCS anvils

D. Bouniol,[a]* J. Delanoë,[b] C. Duroure,[c] A. Protat,[d] V. Giraud[c] and G. Penide[c]

[a]*GAME/CNRM, CNRS/Météo-France, Toulouse, France*
[b]*Meteorology Department, University of Reading, Reading, United Kingdom*
[c]*LaMP, CNRS, Clermont-Ferrand, France*
[d]*CAWRC, Melbourne, Australia*

ABSTRACT: Deep convection in the Tropics is the source of large tropospheric extended clouds usually called anvils. These anvils may produce precipitation (stratiform region of deep convective storms), and also cirrus shields persisting from several hours to several days. Anvils impact the radiation budget, they induce a storage term in the whole water budget which is still relatively poorly quantified, and dynamical feedbacks may be induced in the upper troposphere. The AMMA field campaign which was held over West Africa during the 2006 wet season provided a unique opportunity to document the microphysics of these anvils from unprecedented airborne observations.

Airborne *in situ* measurements of ice crystals and observations from a 95 GHz Doppler radar are used to characterize the microphysical properties of tropical anvils. The dataset is binned into stratiform and cirriform regions. Some data in the stratiform regions were likely obtained close enough to convective cores that the particles may have grown primarily within those cores. The data obtained over the continent and over the ocean are also characterized separately. Particle habit and growth processes are inferred from an examination of the collected particle images, from quantitative comparisons of 95 GHz reflectivities calculated from the *in situ* microphysical observations with the measured radar reflectivities, and from a statistical analysis of the two-dimensional particle images. The predominant precipitation particles above the 0°C isotherm in the stratiform anvil region are rimed aggregates. These rimed aggregates seem to get less dense and of smaller diameter when moving rearward of the system towards the cirriform region. The retrieved density laws (assumed to be power laws) lie close to the relationship for rimed particles of Locatelli and Hobbs.

Particle size distributions in tropical anvils are also studied. The exponential shape seems to be a good approximation for these particle size distributions overall. The decrease in concentration with diameter is also found to be faster for cirriform regions than for stratiform regions. Normalising these particle size distributions produces a relatively invariant shape (in agreement with earlier studies), with however an increased variability for the smallest and largest values of the normalised diameter.

The characterisation of the bulk microphysical properties using these *in situ* microphysical observations shows that the ice water content, the effective radius and the reflectivity-weighted fall velocity generally increase with air temperature, in agreement with earlier studies. These parameters are found to be systematically smaller on average in cirriform regions than in stratiform regions, and this is true at all temperatures. These values are then compared with statistical relationships used in cloud-resolving models and general circulation models, since a realistic representation of microphysics in models is very important to understand not only the processes at work, but the dynamical feedbacks and effects on climate. Large differences are found, the current parametrizations being unable to reproduce the large values of the considered microphysical parameters.

KEY WORDS ice particle density; *in-situ* measurements; airborne cloud radar; AMMA

Received 14 January 2009; Revised 6 November 2009; Accepted 10 November 2009

1. Introduction

Tropical deep convection is the ultimate source of extended clouds, i.e. tropical anvils (Houze, 1977, 1982; Webster and Stephens, 1980; Caniaux *et al.*, 1994; Mace *et al.*, 2006; Cetrone and Houze, 2009). The anvil lifetime, typically 6–12 hours (Leary and Houze, 1980; Ackerman *et al.*, 1988), exceeds the duration of deep convection (that may itself last several hours and even as long as a day) by many hours (Houze, 1989). Far from the active centre of the convective core, the anvil structure becomes optically thinner but still has significant radiative and chemical impacts. The microphysics of crystals in this type of cloud is an important parameter impacting the radiation budget, the amount of water stored in the ice phase (that may lead to precipitation) within the troposphere, and chemical concentrations for both soluble species and species that adsorb onto ice. Regarding more specifically the African monsoon mechanisms, the convective anvils are expected to play a significant role in modulating some of the monsoon components (e.g. modulation of the subtropical jet, warming of the upper troposphere, modification of the radiative budget, dynamical feedbacks with the convective part of the squall lines, moistening of the environment of the convective anvils,

*Correspondence to: D. Bouniol, CNRM/GAME, CNRS/Météo-France, 42 avenue Gaspard Coriolis, 31057 Toulouse Cedex, France E-mail: dominique.bouniol@meteo.fr

modification of the precipitation efficiency...) through their modification of the atmospheric dynamics on a large area. Then, through the strong modulation of radiation at ground level, the surface fluxes will be subsequently modified, which will have a strong impact on the re-evaporation of water at the ground (the so-called 'recycling' process).

During the African Monsoon Multidisciplinary Analysis (AMMA) campaign, a Special Observing Period (Redelsperger *et al.*, 2006) was dedicated to the microphysical characterisation of the Mesoscale Convective System (hereafter MCS) anvils. It is known that convective upward motions are more intense over land than over the ocean (Zipser and LeMone, 1980) and therefore differences in cloud microphysics may be expected. These two regions were sampled during AMMA: with the first part of the field experiment (5–15 September 2006) dedicated to continental MCSs (with an aircraft based in Niamey, Niger), and the second (16–30 September 2006) dedicated to MCSs propagating into a coastal environment (with an aircraft based in Dakar, Senegal). A documentation of the microphysical characteristics of these anvils was performed using a set of *in situ* measurements onboard the French Falcon 20 (2D-P, 2D-C, 1D-P, FSSP, covering a size range of ice particles from 3 μm to 6000 μm). In order to extend this documentation to a vertical cross-section and to describe the internal organisation of the anvils, remote-sensing measurements from a 94 GHz Doppler radar (sampling the anvils with downward and upward-looking antennas) and from a triple-wavelength lidar (355, 532, 1064 nm) were also implemented on the same platform. Several types of MCSs were sampled during this two-phase experiment: large-scale long-lived continental systems, sporadic convection (continental and coastal) and systems arriving over the ocean. Particular attention will be given to characterising the region of the system (stratiform or cirriform) that has been sampled during a particular flight. Large differences may be expected in microphysical properties owing to the processes acting in the various regions and to different updraught intensities producing different ice particle growths (e.g. Stith *et al.*, 2004).

The scientific objective of this paper is to analyse these observations in order to characterise the microphysical properties of the West African anvils.

In the second section, the collected airborne dataset and the meteorological environment of these observations are described. In the third section, *in situ* and radar measurements are analysed to determine the most representative types of hydrometeors sampled in different parts of the anvils and their density as a function of their maximum diameter. Two complementary analyses are conducted to address this objective. The first analysis consists in estimating a radar reflectivity from the microphysical particle size distributions, assuming different particle density–diameter relationships. The computed reflectivities are then directly compared to the radar measurements to indirectly estimate which density law best reproduces the radar observations. Second, a two-dimensional (2D) analysis of 2D-C images is performed by seeking a power-law relationship between the surface and the perimeter of each 2D-C image, assuming that the value of the power-law exponent is related to the ice growth process. In the fourth section, particle size distributions (PSDs) are derived and binned as a function of air temperature, and also as a function of where the measurements have been taken in the sampled systems (stratiform or cirriform regions, and also ocean versus land environments). Since it is well known that PSDs and drop size distributions (DSDs) are highly variable even within a single cloud (e.g. Testud *et al.*, 2001; Delanoë *et al.*, 2005), the representation of the PSD using a single analytical expression (parametrized by one or more parameters) is rather difficult. To overcome this difficulty, a normalisation process (Testud *et al.* (2001), generalised to the ice phase by Delanoë *et al.* (2005)) is applied and the resulting shape function of the normalised PSDs is studied. In the fifth section, the bulk microphysical and radiative parameters of the tropical ice anvils produced by deep convection (ice water content, effective radius and fall velocity) are derived using the ice particle density laws derived in the third section and analysed. Existing trends are identified and existing model parametrizations are evaluated against these retrieved values. Concluding remarks are given in the final section.

2. Description of the Dataset

The present study makes use of 95 GHz Doppler radar measurements and a set of *in situ* microphysical and thermodynamic measurements performed onboard the French Falcon 20 (hereafter F-F20) aircraft.

The RASTA (French acronym: Radar Aéroporté et Sol de Télédétection des propriétés nuAgeuses: Protat *et al.*, 2004) radar is a multi-antenna (three antennas downward, two antennas upward) 95 GHz Doppler cloud radar. Radar calibration was performed during a dedicated flight over the ocean (following the technique proposed by Li *et al.* (2005)) on 28 September 2006. This technique is expected to produce a calibration accurate to within 1 dB or so (e.g. Li *et al.*, 2005). Its application to the present experiment (including technical characteristics) has been detailed in Bouniol *et al.* (2008). These RASTA radar observations have also been compared with the CloudSat radar reflectivities using direct underflights of the CloudSat track (Stephens *et al.*, 2002), showing very good agreement for both ocean surface backscatter and ice cloud reflectivity comparisons (Protat *et al.*, 2009). During AMMA, the radar switches from one antenna to the next in 0.5 s and then takes a total of 2.5 s to sweep through the five antennas with a gate length of 60 m. A major issue for this field campaign was the degraded RASTA sensitivity (Bouniol *et al.*, 2008) estimated as −6.6 dBZ at 1 km for the nadir-looking antenna, −9.0 dBZ at 1 km for the upward-looking antenna, −2.4 dBZ at 1 km for the down-backward antenna, 1.9 dBZ at 1 km for down transverse

antenna, and 2.3 dBZ at 1 km for the up-backward antenna. This sensitivity is not sufficient to investigate the microphysical and radiative properties of the vast majority of thin cirrus from decaying anvil clouds but is sufficient for the investigation of the ice anvil of the MCSs.

The data recorded by the microphysical *in situ* probes consist of 2D images of the individual cloud particles. The analysis techniques use standard algorithms (Heymsfield and Parrish, 1986) applied to the image of each particle to identify the particle shape and size allowing for construction of the PSD at a given time resolution. The diameter for non-spherical particles is computed as the surface equivalent circle diameter (also called 'maximum' diameter, which will be referred to as diameter in the following). For AMMA, a composite spectrum has been built at the 1 s resolution from the 2D-C (sampling from 25 to 750 µm with a 25 µm bin resolution) and from 2D-P probes (sampling from 200 to 6000 µm with a 200 µm bin resolution). Following Heymsfield *et al.* (2002), composite PSDs are generated from the two probes by making use of the spectrum region for which the size distributions from each probe overlap or where the concentrations are comparable.

During some flights, icing occurred on the 2D-P array (see Bouniol *et al.*, 2008), thereby producing corrupted PSDs. In the icing regions and when possible, the 2D-P data have been replaced by the 1D-P data (mainly during flights 72, 75 and 77, see Table I). To document the smaller particle classes, a Forward Scattering Spectrometer Probe (FSSP, sampling from 3 to 47 µm) was used in the F-F20. However due to acquisition problems, the dataset cannot be used. 2D-C concentrations for particles smaller than 100 microns may also contain large errors due to uncertainties in the probe's sampling volume and are therefore not used in this study. Deng and Mace (2008) argued that in cirrus, the majority of the mass occurs at sizes of several hundred microns. In addition, virtually all studies devoted to cirrus so far have used the same truncations (Field and Heymsfield, 2003; Heymsfield, 2003b; Delanoë *et al.*, 2005; for instance) and the measurement of small crystal concentration remains controversial due to the recently-discovered shattering effect on the protruding tips of the probes (Korolev and Isaac, 2005; Field *et al.*, 2006; Heymsfield *et al.*, 2007; McFarquhar *et al.*, 2007). Cloud systems sampled in the framework of AMMA correspond to deeper clouds for which higher ice water contents are expected. The results derived in this study should therefore be less affected by the omission of small particle concentrations than the cirrus studies (where smaller crystals are expected). The physical interpretation of radiative parameters from this dataset must be done cautiously since the lack of particles in the 3 to 100 µm range will lead to an overestimation of the mean size of the crystal and an underestimation of the visible extinction. Zender and Kielh (1994) have shown for tropical cirrus clouds at temperature lower than -40°C, that the truncation of the distribution for particles lower than 20 µm (for a given ice water content (IWC), for which they represent less than 2%) was producing persistent changes in heating rates, albedos and cloud forcing larger than 10%. This overestimation is expected to decrease toward cloud base (Heymsfield, 2003b).

Table I summarises the seven flights with microphysical objectives (and usable datasets) during the AMMA experiment. Five flights were performed over the continent (the first four in the Sahel region and one east of Dakar) and the remaining two correspond to coastal and oceanic cloud systems. Documenting the microphysics of the anvil is challenging, since strong heterogeneities exist within the cloud shield. It is very important to know where the measurements were taken with respect to the main convection cores and when they are located in the cloud system life cycle. Heymsfield *et al.* (2002) also stressed the problem of horizontal cloud heterogeneity and suggested using a Lagrangian spiral to characterise the vertical variability of a given cloud system by deriving a vertical profile. This flight strategy was not adopted for the AMMA experiment since the payload of the aircraft, with simultaneous *in situ* and remote-sensing measurements provides a documentation of the vertical distribution of the ice cloud properties. It has rather been chosen to cover a horizontal domain as large as possible in order to obtain a three-dimensional view of the system. However, even within a given flight, data were collected at different altitudes, which is information that can be exploited for the *in situ* observations.

Before studying the microphysical properties, insights into the life cycle of the various cloud systems sampled must be gained. To do so, a useful tool is the geostationary imagery that provides an image over the West African zone every 15 minutes. Figures 1 and 2 show Meteosat Seconde Génération (MSG) images in the 10.8 µm channel at different selected times of each MCS's life cycle. To better describe the life cycle, the outputs of a tracking algorithm (Arnaud *et al.*, 1992; Mathon and Laurent, 2001; Fiolleau *et al.*, 2009) have been used. The technique consists in delineating continuous clusters in the full-resolution infrared imagery by using a single brightness threshold. Using an overlap assumption, clusters are then identified from one image to another and followed in time. The morphology (spatial extension, brightness temperature distribution. . .) of the cold cloud shield is hence characterised over the life cycle of the associated MCS. The tracking algorithm attributes a number to each cloud cluster that allows an easy identification in the images (these numbers are also reported in Table I). For each sampled cell, the surface area of the tracked cloud shield is shown at two different infrared temperatures as an indicator of the horizontal extent (233 K contour, in red) and of the colder region (213 K contour, in green). The growing, mature and decaying phases and duration of the cloud system are observable in the first panel in Figure 1 for flights in the Niamey region, and in Figure 2 for flights in the Dakar region. When another cell merges with the tracked cell, a black cross appears on the red line indicating that the increase in cloud cover is associated with the inclusion of a cell. Several lines are superimposed in this panel. First the yellow shaded surface

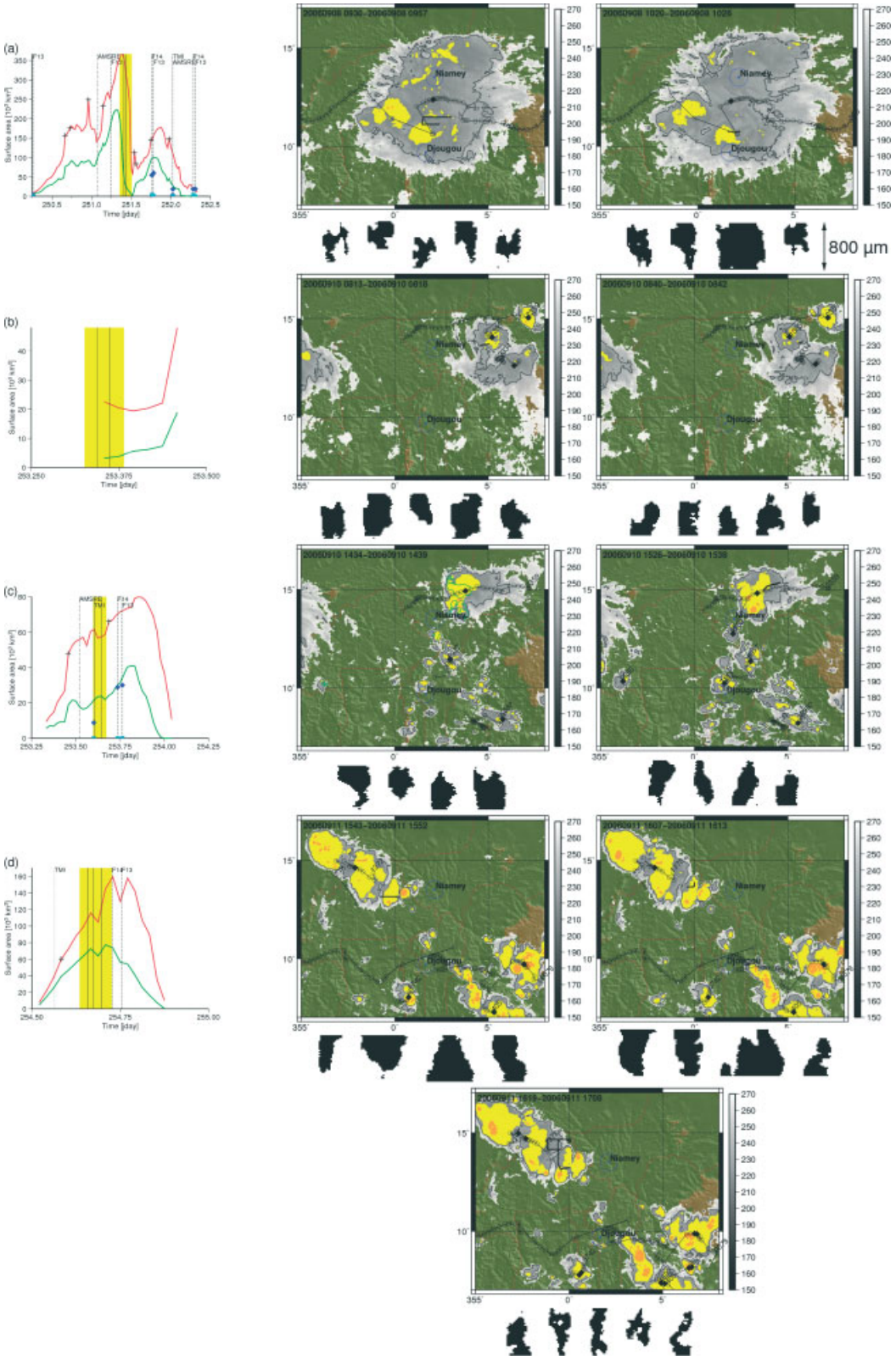

Figure 1. Description of the life cycle and cloudiness situation for each sampled cloud system and each segment performed by the F20 in the Niamey region with (a) flight 59, (b) flight 62, (c) flight 63 and (d) flight 64. For each cloud system, the life cycle as obtained by the MSG tracking algorithm is shown, with surface area of MSG 10.8 µm brightness temperature lower than 233 K in red, and lower than 213 K in green. Dash, dotted and dash-dotted vertical lines represents overpass of microwave radiometers: TMI (TRMM), SSM/I (F13 and F14) and AMSRE (Aqua) respectively. When the MSG 233 K contour is fully enclosed in the radiometer swath the PCT surface area lower than 250 K are reported on the corresponding line with a dark blue diamond, or a light blue square for PCT lower than 150 K. The yellow square corresponds to the flight time with black solid line symbolising the segment time. The following images (one per segment) are MSG 10.8 µm brightness temperature (in K, grey level) threshold at 270 K and superimposed on a geographical map. The black contour shows the iso-233 K. Temperatures lower than 213 K are shown in yellow, those lower than 200 K in orange. When microwave radiometer overpass exists, green contour corresponds to the iso-PCT 250 K and red contour to 150 K. The system barycentre trajectory as obtained by the tracking algorithm is shown with linked symbols, and each system is numbered. The ground-based radar's location is also indicated by an open circle. The F20 trajectory during the segment is shown as a bold black solid line. For each segment a short sample of typical particle images from the 2D-C probe (each pixel being approximately 25×25 µm^2) is shown.

Table I. List of AMMA flights with microphysical objectives where *in situ* microphysical measurements and radar measurements have been collected at the same time

Flight number/tracking number Flight date Time (hours)	Location/Flight objectives	Available data	Segment time (hours)/Temperature (°C)
Fig. 1(a): 59/395 08 September 2006 8.7–12.16	Continental/Large scale MCS in decaying phase	S1: cirriform S2: stratiform/some icing on instruments	S1: 9.501–9.951/−45.36 S2: 10.34–10.43/−47.22
Fig. 1(b): 62/1365 10 September 2006 7.83–9.16	Continental/MCS in growing phase	S1: stratiform/some icing S2: cirriform	S1: 8.225–8.305/−18.28 S2: 8.683–8.7/−37.55
Fig. 1(c): 63/2359 10 September 2006 14.37–16.15	Continental/MCS in growing phase	S1: stratiform S2: cirriform/some icing on instruments	S1: 14.565–14.6505/−17.81 S2: 15.47–15.64/−33.79
Fig. 1(d): 64/1372 11 September 2006 15.26–17.44	Continental/Cell at the rear of larger size MCS, rapidly evolving	S1: stratiform S2: stratiform/some icing on instruments S3: cirriform	S1: 15.72–15.86/−37.33 S2:16.12–16.215/−37.62 S3: 16.322–17.13/−37.49
Fig. 2(a): 72/5174 22 September 2006 13.83–16.90	Coastal + Continental/A-Train overpass within precipitating system in mature phase	S1: stratiform S2: cirriform S3: stratiform S4: cirriform S5: stratiform	S1: 14.32–14.7/−17.60 S2: 14.7–15.354/−17.28 S3: 15.354–15.7/−17.46 S4: 15.7–15.85/−17.67 S5: 15.85–16.38/−17.65
Fig. 2(b): 75/2427 26 September 2006 9.78–12.6	Oceanic/Exporting MCS	S1: stratiform S2: stratiform S3: cirriform	S1: 10.57–10.85/−16.85 S2: 10.85–11.15/−17.10 S3: 11.36–11.64/−17.47
Fig. 2(c): 77/7506 27 September 2006 13.25–16.0	Oceanic/Exporting MCS	S1: stratiform	S1: 13.56–13.72/−29.16

2009Dec04 074138

corresponds to an F-F20 mission, indicating which phase of the life cycle is documented. The dashed, dotted and dash-dotted lines correspond to overpasses by spaceborne microwave radiometers TMI (TRMM) (Tropical Rainfall Measuring Mission Microwave Imager), SSM/I (F13 and F14)(Special Sensor Microwave/Imager) and AMSRE (Aqua)(Advanced Microwave Scanning Radiometer E), respectively. The more rigorous way of locating convective and stratiform regions within a cloud shield is to use thresholds (Mohr and Zipser, 1996) in Polarisation Cross Temperature (PCT). When possible (i.e. when the system of interest is fully located in the microwave radiometer swath) the surface areas of PCT lower than 250 K, which characterise the stratiform regions and differentiate them from surrounding cirriform regions (Mohr and Zipser, 1996), are computed and reported as dark blue diamonds in the first panel. The surface areas with PCT lower than 150 K (characterising strong deep convection regions according to Cecil *et al.* (2005)) are also shown as light blue squares. When there is a common sampling by MSG and the microwave radiometers over a given system, it appears that both measurements provide a very similar evolution of the cloud systems. The system sampled during Flight 62 (Figure 1(b)) is characterised by a short lifetime (3 hours) and only a growing phase. Its life cycle ends by a merging at 1130 UTC with the system number 2359 (see Table I), sampled during Flight 63, as shown by the black cross in the 233 K surface area in Figure 1(c), left panel. Therefore two distinct regions of the system 2359 were sampled with the F-F20 at two different times of its life cycle.

One of the aims of this paper is to provide typical values of microphysical and radiative properties of anvil clouds (ice water content, fall velocity, and effective radius). For this purpose, the different flights are separated according to the cloud region and/or the flight altitude. While the separation by altitude is an objective criterion, the separation by similar regions (stratiform, cirriform) in the different clouds is trickier, as there is no objective criterion available. Since there is generally no overpass of microwave radiometer available as the aircraft flew in the clouds, the MSG brightness temperature was used as a 'proxy' of convective activity in order to separate the flights into segments. The cold region

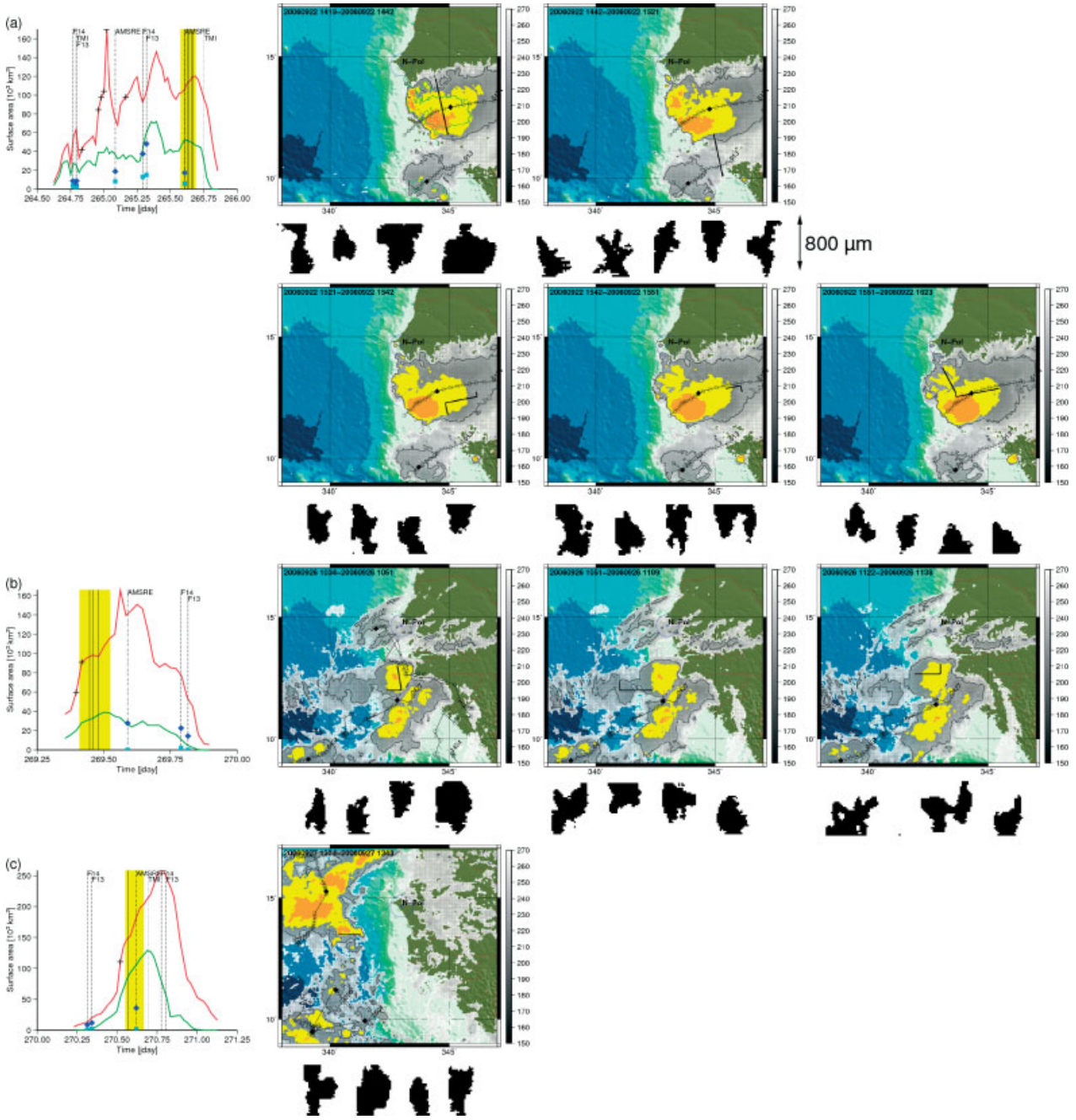

Figure 2. Same as Figure 1 but for flights in the Dakar region with (a) flight 72, (b) flight 75 and (c) flight 77.

(213 K), even if generally larger than the stratiform region (according to the PCT definition, see comparison of blue diamonds with green curve in Figures 1 and 2, first panel), has been used to locate what is called the stratiform region within the cloud shield, an unknown fraction of which may be rather close to convective cores. The remaining region of the cloud shield (larger 233 K) is called hereafter the cirriform region.

Each segment (denoted S in Table I) was extracted for each flight where the aircraft was flying at constant altitude (or nearly constant temperature) and sampled only one defined cloud region with usable data (i.e. at least one part of the segment does not present instrumental icing). The time intervals corresponding to each segment are given in Table I. State parameters (dynamical and thermodynamic measurements) were provided from the aircraft's standard suite of instruments. The mean temperature is given for each segment in the last column of Table I.

The flight track during each segment is shown in Figures 1 and 2 (black solid line), superimposed on the MSG infrared (10.8 µm) channel image. Typical 2D-C particle images are also shown below each panel. The MSG images have a threshold at 270 K and the lower brightness temperatures are shown in grey levels (233 K is shown by the black contour). Temperatures lower than 213 K are shown in yellow, and those lower than 200 K in orange. Figure 1 and 2 show that different system types (in size, region or stage in their

life cycle) have been sampled, with avoidance of the most active convective regions (if it is assumed that the intense ascending motions are collocated with the colder brightness temperature, shown in orange in Figures 1 and 2) for safety reasons. Following Mohr and Zipser (1996), PCT lower than 250 K may be associated with moderate rain (larger than 3 mm h^{-1}). By extension, we may then assume that regions associated with MSG brightness temperature lower than 213 K corresponds to precipitating regions. All the flight segments presented in this study have then been sorted using the MSG images and the outcome of this classification is given in Table I.

Our intention was to include only stratiform and cirriform anvil ice cloud properties in the present dataset, although it is likely that some segments were quite close to intense convective regions (see for instance the first segment of Figure 2(a) where an AMSRE onboard Aqua overpassed the system at the same time the aircraft was in the area). Other means exist (such as ground-based radar) and were deployed during the AMMA campaign (Redelsperger *et al.*, 2006) in order to document the convective region of the MCSs. In particular, two polarimetric Doppler radars were deployed in north Benin (Djougou site, see Figure 1) and the other in the Dakar region (N-Pol radar, see Figure 2). The polarimetric signal from these radars can be used to infer microphysical properties of the MCSs. However, even if very sensitive, these radars' capabilities remain insufficiently sensitive in particular to document the cirriform anvils for which our dataset is particularly valuable. In addition to these two polarimetric radars, the MIT C-band Doppler radar was also deployed at the Niamey site (see Figure 1).

Figure 3(a) shows the mean vertical profiles of reflectivity (computed as the average of reflectivity values at a given height) provided by the nadir and the upward-looking antennas of the RASTA radar for each individual segment listed in Table I. A large spread in the shape of the profiles is observed in Figure 3(a). It is noteworthy that all profiles exhibit the same general trend of decrease in reflectivity with height. The dataset is separated according to the previously described stratiform/cirriform classification, and re-plotted using the same colour code in Figure 3(b) and (c) respectively. Two distinct behaviours are observed: the cirriform profiles show a decrease in reflectivity with height while others present a decrease in reflectivity with increasing distance from the radar or rather constant reflectivity profiles that may signal possible attenuation. Within these profiles, the melting level is identifiable (by a local 'step' in the reflectivity profile). From looking at ground-based 94 GHz radar profiles from the Atmospheric Radiation Measurement (ARM) Mobile Facility (installed at Niamey) and from the conceptual schemes of anvils, a decrease of the reflectivity values toward the cloud base is expected for cirriform segments since such regions do not produce precipitation. The cirriform profile of Flight 64 in Figure 3(c) is a good illustration of this 'expected' shape. The different shapes of the other profiles may be explained by the way the profiles are built. These are averaged profiles over temporal segments. Therefore even if very few profiles display a step in the reflectivity profile indicating the melting level (or data at relative low altitudes), they appear in the resulting profile. It does not mean that precipitation exists throughout the segment in such profiles.

3. Analysis of the Microphysical Dataset

The main parameter responsible for the natural variability of the microphysical and radiative properties within ice clouds is the particle habit. Therefore it is a major issue to infer which type of particle is most often encountered

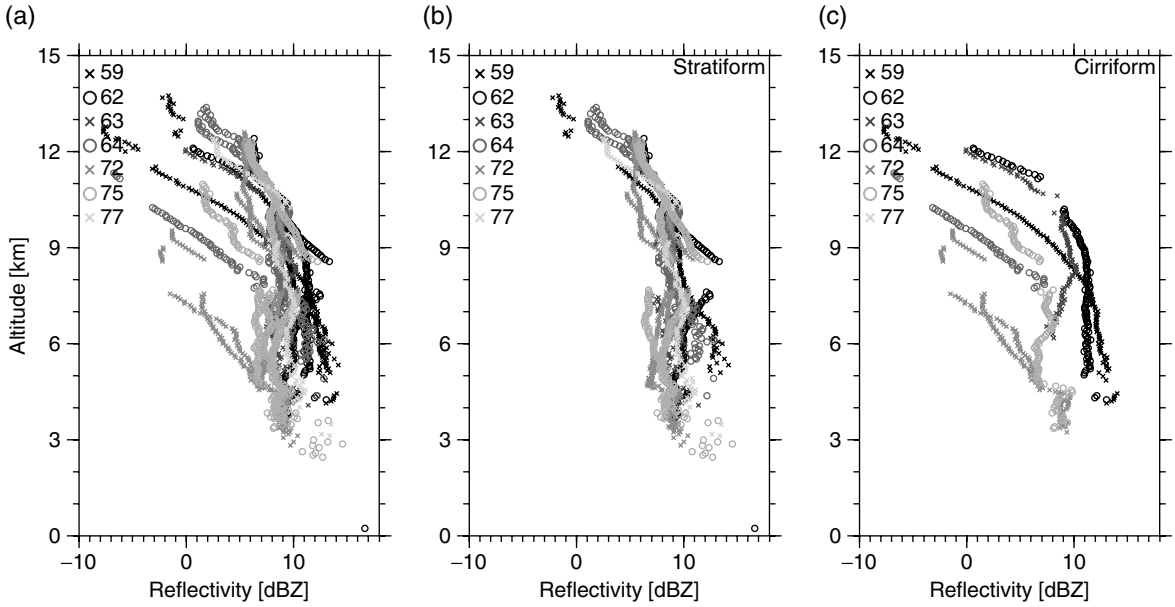

Figure 3. Mean profile of reflectivity in dBZ as a function of altitude in km for the flight segments listed in Table I. Each grey level corresponds to a different flight number with (a) all profiles, (b) stratiform profiles and (c) cirriform profiles. See text for the definition of stratiform and cirriform.

within the various regions of the tropical ice anvils sampled during AMMA. This is also mandatory if one wants to accurately identify which process is playing a role in the anvil life cycle and quantify the typical values of radiative and microphysical parameters in such systems.

Some insights about the most representative types of ice particle encountered in the various regions of the cloud systems can be first obtained from a visual examination of 2D-C images shown in Figures 1 and 2. An overall examination would classify most observed hydrometeors as undetermined shape and would conclude that smaller diameters are present within cirriform regions. A more careful examination (separating in particular stratiform and cirriform regions, see Table I) reveals that less dense hydrometeors are present within the cirriform region with more complicated shapes and inclusion of holes within the 2D images. Particles observed in the stratiform regions correspond to complex-shaped rimed crystals and aggregates of rimed crystals comparable to those described in Heymsfield *et al.* (2002) in a deep anvil during the Large-scale Biosphere–Atmosphere experiment (LBA) in Brazil. There were no supercooled water measurements included in the experimental design of AMMA and therefore the regions where the riming occurred could not be clearly identified. However, due to the range of temperatures sampled (-16 to -45°C) it is likely that riming had been occurring in the convective region and the particles were then advected into the anvil by the upper-level outflow. Bullet-rosettes were only observed at the very edge of cirriform regions (not shown). This indicates that the majority of the particles sampled in the cirriform regions are related to generation processes different from those activated in synoptically generated cirrus that are characterized by very large occurrences of bullet-rosettes. Finally no vapour-grown crystals (columns, capped columns, hexagonal plates or branched crystals) that generally correspond to sixfold symmetry crystals (Pruppacher and Klett, 1978) were identified in the 2D-C images.

Complementing this visual examination, two different analyses are applied to the AMMA dataset in order to more objectively establish the most probable growth process of the particle and the associated density–maximum diameter relationship.

3.1. Density–maximum diameter retrieval

The calculation of the various microphysical and radiative parameters requires the knowledge of the relationships between the ice particle density and mass as a function of the maximum particle diameter, notated $\rho(D)$ (Heymsfield *et al.*, 2004). Unfortunately, during the AMMA experiment, no probe such as the Cloud Particle Imager (CPI) was available onboard the aircraft to determine the distribution of particle habits, mainly due to the space and power limitations of the F-F20. An indirect method is therefore used in what follows to get an estimate of the most representative particle habit in the stratiform and cirriform regions of the West African MCSs. To do so the reflectivity measured by the 95 GHz radar onboard the F-F20 is compared to that calculated from the PSD measured by the *in situ* probes and a set of $\rho(D)$ relationships of the literature. The ice particle density (in g cm^{-3}), is expressed as a power law based on diameter, $\rho(D) = a\ D^b$ (with D in mm). Such a relationship is widely used in order to represent the decrease of density with increasing diameter (see for instance the early work of Zikmunda and Vali (1972) or Heymsfield (1972)), b being generally negative. Exceptions are noted for some graupel-type particles, where $\rho(D)$ can increase with size (Heymsfield and Kajikawa, 1987). A limit diameter (D_l with $\rho_\mathrm{ice} = a\ D_\mathrm{l}{}^b$) under which the obtained density exceeds the density of solid ice ($\rho_\mathrm{ice} = 0.917$ g cm^{-3}) is introduced, following Heymsfield *et al.* (2007). The solid ice density is used in the calculation when the ice particle diameter is less than this limit diameter. Figure 4(a) shows a graphic representation of D_l values (lines) in a 2D space with the a coefficient on the x-axis and the b coefficient on the y-axis. The $\rho(D)$ relationships published in the literature (Locatelli and Hobbs, 1974; Mitchell, 1996; Brown and Francis, 1995; Francis *et al.*, 1998; Heymsfield *et al.*, 2004) are superimposed in this diagram. All literature laws are corresponding to D_l lower or equal to 100 μm defining half of the array (upper left corner) where the density can be predicted. A 100 μm threshold thus appears as a reasonable limit for defining the domain where the a and b coefficients can be sought.

A 95 GHz reflectivity is computed using the *in situ* measurements for each pair (a,b) according to the following expression:

$$Z_\mathrm{e} = \frac{\lambda^4 10^{18}}{|K_\mathrm{w}|^2\ \pi^5} \int N(D_\mathrm{eq}) \sigma_\mathrm{bsc}(D_\mathrm{eq}, \lambda) \mathrm{d}D_\mathrm{eq} \qquad (1)$$

where Z_e is the equivalent reflectivity factor expressed in mm^{6}m^{-1} and converted to dBZ by taking 10 log of Eq. (1), λ is the wavelength (3.21 mm in the present case), K_w is the refractive index of water (that depends on temperature and λ), N is the PSD, σ_bsc the surface backscattering cross-section and D_eq the 'equivalent melted diameter' (i.e. the diameter a liquid droplet of the same mass as the ice particle would have, see Testud *et al.* (2001) or Delanoë *et al.* (2005) for further details). Each diameter bin is converted to an equivalent melted diameter ($D_\mathrm{eq} = (\rho(D)/\rho_\mathrm{water})^{1/3} D$) using the ice-diameter density. The corresponding σ_bsc is computed using Mie theory and makes use of the refractive index of ice K_i that also depends on the ice density. Donovan *et al.* (2004) demonstrated using discrete dipole approximation (DDA) that for spherical particles (or equivalent spherical particles), the Mie theory could be employed for accurate calculation of radiative or microphysical parameters as a good compromise between an exact calculation (but very costly in computation time) and the Rayleigh approximation (not accurate enough). They estimate the differences in reflectivity between DDA and Mie calculation for single particle population generally below 20% for hexagonal columns and stellar crystals and below 30% for plates (in linear units). The (a,b) pair for which the difference

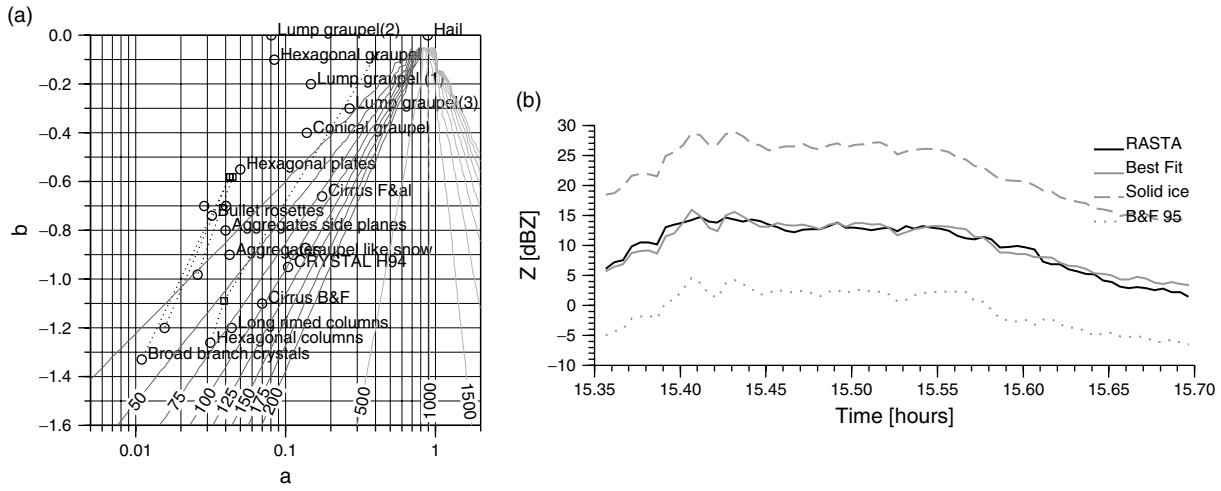

Figure 4. (a) Two-dimensional representation of the density law expressed as a power law: aD^b with D in mm and the density in g cm^{-3}. Lines represent iso-values of limit diameter D_l (see text for explanation). Density laws from the literature (not all labelled) are superimposed in this diagram: conical graupel, hexagonal graupel, graupel-like snow and lump graupel (2) and (3) from Locatelli and Hobbs (1974), cirrus from Brown and Francis (1995) and Francis *et al.* (1998), CRYSTAL H94 from Heymsfield (2004) for low-latitude convectively generated ice cloud layers and the remaining ones from the synthesis paper of Mitchell (1996). Symbols linked by dotted lines belong to the same particle habit but for different diameter ranges (larger symbols corresponding to larger diameter range and cross for smaller diameter, square for mid-size and circle for the larger or when no separation in diameter classes exists). (b) Comparison of the computed reflectivity (grey lines) for the flight 72 S4 with the RASTA reflectivity (solid black line). Three simulated reflectivities are shown; Best Fit (solid grey line) corresponding to the simulated reflectivity for the (a,b) pair that minimises in the least-square senses the difference with the measured reflectivity, the simulated reflectivity using the density for solid ice particles (dashed grey line) and the simulated reflectivity using the Brown and Francis (1995) density law (dotted grey line).

(in the least-squares sense) between the measured and the simulated reflectivity is minimum is retained as the most representative $\rho(D)$ relationship for a given flight segment. The process is repeated for each flight segment. It could be argued that this method might be questionable because the particles dominating the reflectivities (measured or re-computed from *in situ* measurements) are located at the larger end of the PSDs. However at 94 GHz, for relatively large particles, the Mie effect does reduce the dependency on size since reflectivity cannot be any longer considered as the sixth power of particle size, but a lower power depending on size itself and the density−diameter relationship. This retrieval process is illustrated in Figure 4(b) where the measured reflectivity (the closest to the aircraft in black) is shown for the fourth segment of flight 72 (see Table I). The first usable gate in the RASTA system is located at 240 m from the aircraft (see Bouniol *et al.*, 2008), however to ensure a good quality of the reflectivity measurements the reflectivity from radar gate 9 (540 m) is used in this study assuming that attenuation does not occur. To ensure this point, reflectivity measurements from above and below the aircraft have been compared and the comparison process is also repeated for the two following gates. The simulated reflectivity time series for the (a,b) pair that minimises the difference in a least-squares sense between observations and simulations is shown in solid grey. In order to highlight the variability that may be expected by changing the $\rho(D)$ relationship in these calculations, the reflectivity time series using the Brown and Francis (1995) $\rho(D)$ relationship ($\rho(D) = 0.07\ D^{-1.1}$ with D in mm, in dotted grey) and the solid ice assumption (in dashed grey) are also shown. The Brown and Francis (1995) relationship is identical to the Locatelli and Hobbs (1974) relationship for aggregates of unrimed radiating assemblages of plates. It is widely used in radar−lidar retrievals. It appears from this example that this relationship may not be adapted for the radar−lidar retrieval of the West African anvils.

The $\rho(D)$ relationships producing the smallest difference for each segment are depicted in Figure 5(a), overlaying those from the literature discussed previously in Figure 4(a). It must be noted that the reported $\rho(D)$ relationships do not necessarily correspond to particles sampled in the same situations. For instance the relationships for the various graupel particles are coming from the Locatelli and Hobbs (1974) measurements collected in the early 1970s winter in the Cascade Mountains of Washington at altitudes of 750 and 1500 m above sea level. Differences in thermodynamic profiles may lead to different formation processes for ice particles (see Cetrone and Houze, 2009) and particle density will be different depending on the sampled system. Williams and Zhang (1996) highlight this point for rimed particles. These 'classical' laws are well organised in the two dimensional (a,b) space with rimed particles located in the top right corner, columns or cirrus particles of Brown and Francis (1995) at the bottom and aggregates being located in the middle region of the domains. The exponent b of the diameter density law represents the decrease in density as size increases. Heymsfield *et al.* (2007) noted that increasing b reduces ρ for smaller particles and increases it for larger ones. The a coefficient fixes the range of density. All the retrieved $\rho(D)$ are located in the upper-right corner, i.e. in the region of the 2D-space where were located the $\rho(D)$ for rimed particles. The relatively high values of a lead to density values in the range 0.1 to 0.8 g cm^{-3}

(depending of the diameter), in the range of natural rime proposed by Macklin (1962). This range corresponds to density encountered for rimed particles by Williams and Zhang (1996). Heymsfield *et al.* (2004) found mean density value of 0.2 to 0.3 g cm^{-3} (between 8 and 10.5 km) in CRYSTAL-FACE (Cirrus Regional Study of Tropical Anvils and Cirrus Layers – Florida Area Cirrus Experiment) anvils. In this dataset dedicated to convectively generated anvils, aggregates were the dominant particle habit with however rimed particles observed at temperature as low as −50°C. They also found mean density as large as 0.5 g cm^{-3} (between 4.2 and 6.7 km) in cirrus uncinus where rosettes were the dominant particle habit (their Atmospheric Radiation Measurement, ARM dataset). The retrieved density laws present generally exponent values (b) lower than −0.4 which signifies a more rapid decrease in density with size with respect to the rimed particles of Locatelli and Hobbs (1974). This point agrees with the aspect of individual particles shown in Figures 1 and 2.

Flight 59 segment 1, and flight 62 segments 1 and 2 present the larger (a, b) pair. However Flight 59 segment 1 and flight 62 segment 2 were taken at low temperature (−45.36 and −37.55°C) in cirriform segments. The 2D-C images for these two segments do not correspond to very dense hydrometeors. A plausible explanation of the very large density retrieved in these segments may be the truncation of the PSD for diameters larger than 100 µm. 2D-C images in Figures 1 and 2 have shown that particles look smaller in these segments and according to their temperature high concentration of small particles may be expected at these altitudes (Sherwood, 1999). An overestimation of the density of the particle is then necessary if one wants to be able to match the measured reflectivity. Concerning Flight 62, it may be possible according to the temperature of this segment (−18°C) that the encountered particles were denser with respect to the other segments.

As summarised in Table I, the data were collected at different locations within the cloud system but also at different altitudes (i.e. different air temperatures). To analyse further the retrieved $\rho(D)$ relationships, they are analysed as a function of temperature, Figure 5(b), keeping the exponent b as the y-axis. It is observed in this figure that all the data collected in the Dakar regions correspond to the higher temperatures (about −20°C) and the two segments of flight 59 to the lower temperatures (about −45°C). No particular trend with temperature of the exponent of the $\rho(D)$ relationship is observed in Figure 5(b); for a given temperature the full range of b values is encountered. In contrast, Heymsfield *et al.* (2004) found a systematic decrease in mean density with increasing temperature.

3.2. Analysis of 2D particle populations

Additional indirect information about the particle habits can be obtained from the qualitative inference of their dominant growth mode. Duroure *et al.* (1994) proposed to use for this purpose the 'roughness' exponent, which links the surface area and the perimeter of a population of ice particles. This roughness exponent is a geometrical measurement of the 'complexity' of the image and provides a complementary analysis to that presented in the previous section. The 2D surface area and the perimeter of each particle image (in pixel units, see Duroure *et al.*, 1994) of a given sample are measured and reported as a single point in the perimeter−surface area plane (with log−log scales). The scatter is then fitted with a linear relationship, where the slope is defined as the roughness exponent. Duroure *et al.* (1994) show empirically that this roughness exponent is related to the growth mode. Indeed for riming and low supersaturation vapour deposition growth the surface irregularities (increasing the number of perimeter pixels) always grow linearly with the 2D surface area of the particle. For dendritic (high supersaturation vapour

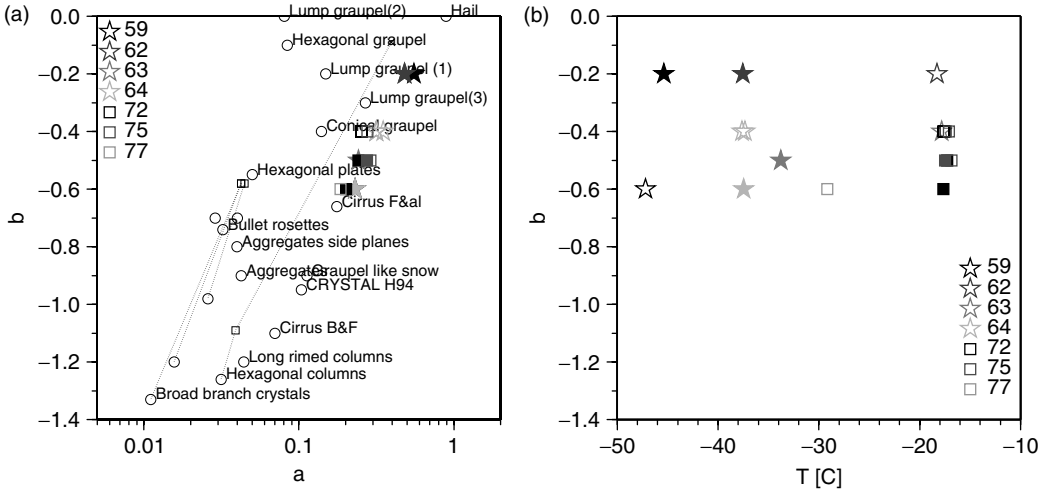

Figure 5. (a)Two-dimensional representation of density laws expressed as a power-law: aD^b with D in mm and the density in g cm^{-3} superimposed on (small black symbols) laws encountered in the literature, see Figure 4(a). (b) Retrieved exponent b of the density law as a function of temperature in °C. Stars with the grey levels (one for each flight) show the retrieved density laws for the Niamey region as squares correspond to flights in the Dakar region. Filled symbols are associated with density laws retrieved in cirriform segments as open symbols show the laws for stratiform segments.

deposition) and agglomeration growths the surface irregularities grow faster than the size of the particle, leading to the number of pixels of the perimeter increasing faster than the number of pixels of the 2D surface area. Two limit cases may be considered: a slope of 0.5 could occur with images from a population of particles formed by the diffusional growth of a single form of simple crystal with fixed growth rate on each axis. A slope larger than 0.5 corresponds to a crystal population in which the complexity is increasing with size (small plate crystals taking on dendritic arms, for instance). The upper bound of this roughness exponent is unity, corresponding to cases where the number of pixels for the perimeter equals the number of pixels of the 2D surface area. A highly rimed particle will have a lower roughness exponent, while particles growing through aggregation will have a higher roughness exponent (values about 0.8).

Each segment of the AMMA flights is analysed using this roughness exponent and a mean value is computed for each segment. Figure 6(a) shows the stratification of this mean roughness parameter as a function of temperature. Two features are observed. First, for temperatures higher than -20°C, a wide range of roughness exponent values is found. The lowest roughness exponents are found for stratiform segments and the highest for cirriform regions. This stratiform/cirriform behaviour may be interpreted as a function of the distance to the deep convection core (according to our conceptual scheme), where rimed particles are detrained from the convective core in the stratiform region (Heymsfield *et al.*, 2002; Cetrone and Houze, 2009). Some data in the stratiform regions were likely obtained close enough to convective cores that the particles may have grown primarily within those cores. This is particularly true for Flight 72 segments (open black square in Figure 6(a)) for which an AMSRE overpass exists and shows PCT lower than 150 K close to the sample region (Figure 2(a)). For temperatures less than -20°C, the roughness exponent of cirriform segments increases with decreasing temperature, suggesting less rimed particles at low temperature in cirriform segments. This observation is in agreement with the less dense hydrometeors found in 2D-C images for cirriform segments (see Figures 1 and 2).

Figure 6(b) shows the exponent of the density–diameter relationship (b) as a function of the roughness parameter. The variability in shape of the observed particles is reduced as may be seen in Figures 1 and 2. However, it appears also that the larger roughness exponents (between 0.65 and 0.7) that would correspond to more complex particle shapes are observed for cirriform segments. Lower roughness exponents (between 0.58 and 0.65) are found within stratiform segments (even at relatively high altitude) suggesting the encountered particles in these segments grown mainly through the riming process. Houze and Betts (1981) proposed rimed aggregates and hexagonal graupel as probable ice particle types just above the melting layer. Their observations from the GARP Atlantic Tropical Experiment (GATE) experiment suggest active anvil clouds, with enough lifting present to maintain liquid water in the presence of ice. The present observations were taken at higher altitudes and it is likely that these rimed hydrometeors originated from the convective updraughts. A low roughness parameter could be due to growth by water deposition, but if that were the case, one would find a rather different predominant density–diameter relationship and different 2D images.

In this section the particle habits encountered within the different segments were investigated. $\rho(D)$ relationships are found to be similar to the rimed particles relationships of Locatelli and Hobbs (1974). However no obvious variability can be established between the $\rho(D)$ relationship and temperature or the segment type (stratiform or cirriform). The analysis of the relationship between surface area and perimeter of individual particles shows that more aggregation occurred in cirriform profiles with respect to stratiform segments where more rimed particles were found, even at relatively high altitudes. These rimed particles may originate from expulsion of rimed particles by the internal dynamics from the convective core to

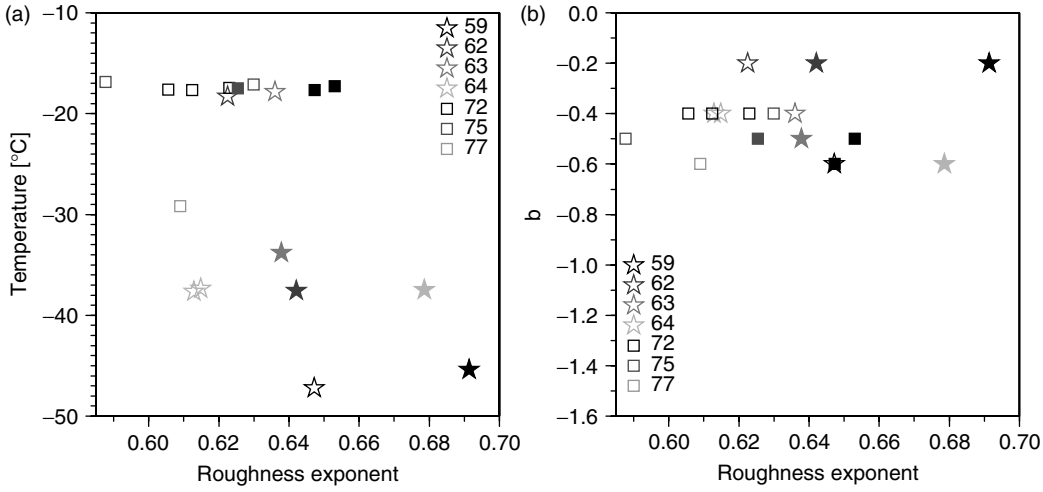

Figure 6. (a) Stratification of the roughness exponent as a function of temperature. (b) Exponent of the density law (b) as a function of the roughness parameter of each flight of the AMMA experiment. Filled symbols correspond to cirriform segments.

the stratiform region, as suggested in Cetrone and Houze (2009) or Heymsfield *et al.* (2002). These results broadly agree with the visual examination of the 2D-C images shown in Figures 1 and 2.

4. Statistical Study of the Particle Size Distribution

The microphysical and radiative cloud properties are related to the particle habits as mentioned earlier on. They are also directly related to the PSD of hydrometeors. The PSD is known to be highly variable from one cloud to another and from one region to another. First, PSD properties are compared between the different segments and from one flight to another. Then, the same properties are investigated after the PSDs are normalised following the Testud *et al.* (2001) normalisation concept generalised for ice clouds by Delanoë *et al.* (2005).

4.1. Variability of the particle size distribution

Figure 7 shows the average PSD for each segment of each flight (one panel per flight). Cirriform and stratiform segments are respectively represented by dashed and solid lines. The main difference between stratiform and cirriform segments appear for the large diameter particles (larger than 200 µm) where cirriform segments exhibit systematically lower concentrations (for a given altitude) than the stratiform segments. This result agrees with the visual examination of the 2D-C images of section 3, where particles appeared to be smaller within cirriform segments. In agreement with Heymsfield *et al.* (2002) and Delanoë *et al.* (2005), it is found that for particles larger than 500 µm for the flight in the Niamey region (a) to (d) and about 800 µm for the flight in the Dakar region (e) to (f) that the concentration (plotted with logarithmic scale) decreased linearly with size (plotted with linear scale), indicating that above these sizes the PSDs are of exponential shape. This linear shape occurred for both stratiform and cirriform segments but, as seen in Figure 7, with a larger slope for the cirriform segments (since concentration of larger particles are reduced in cirriform segments). Generally speaking, for particles smaller than the above-mentioned thresholds, a linear decrease is not obvious (when plotted on a logarithmic scale, not shown), suggesting that the PSDs cannot be represented with a power law in this region (see Heymsfield *et al.*, 2002).

An overall comparison of these PSDs may be performed by accumulating all of them on the same plot as illustrated in Figure 8(a) (on a log−log scale). This figure compares the Niamey region segments in solid lines to the Dakar region segments in dashed lines. If the two segments of flight 59 and one segment of the flight 63 (corresponding to rather low temperatures, about $-45°$C and $-33°$C respectively) are not considered, PSDs measured above the ocean appear less convex than the PSDs measured above the continent, owing to larger concentrations of both small and large particles above the ocean. Two reasons could explain the differences in the tails of the distributions. First, most segments of the oceanic flights were collected at rather 'warm' temperatures (about $-17°$C except for Flight 77 which was collected at $-29°$C, see Table I). Growth processes governing the PSD evolution are then expected to be intrinsically different. Second, Field and Heymsfield (2003) suggest that the evolution of the larger particles in PSDs is driven by aggregation. This would imply that aggregation is more efficient to generate large particles over the ocean than over the continent. This point does not agree with what is found with the roughness exponent results presented in Figure 6(a) which show that the whole range of roughness exponents (0.53 to 0.69) is found for these segments (Flight 72 and 75, squared segments).

As discussed in section 2, 2D-C concentrations may contain large errors for diameters smaller than 100 microns. Therefore quantitative use of those measurements is not possible. Qualitative examinations can however be conducted here. A large quantity of small particles (smaller than 100 µm) is found in continental colder segments, in particular for Flight 59 (with a temperature of about $-45°$C). The origin of this higher concentration of small-size crystals is unknown but this observation suggests that even if a part of the observed particles within these segments is advected from the convective core, another generation process acts to increase the concentration within the well-developed cloud shield (see Figure 1(a)) at high altitude. To confirm this hypothesis, it is interesting to compare the mean PSD obtained from Flight 64 (middle grey in Figure 8) during which the ice anvil of a just-emerging/fast-developing system was sampled (see Figure 1(d) and Table I for a documentation of the life cycle). For this MCS, the more convex PSDs are observed with reduced concentration of small particles, suggesting that most particles are advected from the convective core. This observation (see also Figure 7(d)) is in agreement with Rickenbach *et al.* (2008), who examined an anvil generation in Florida on 23 July 2002 during the CRYSTAL-FACE experiment. They observed a PSD clearly skewed towards large particles close to the convective part and a concentration that decreased steadily when moving away from the convective core. Figure 7 shows also the same results, with for each flight, cirriform segments (thus further from the convective core than stratiform segments) exhibiting lower concentration of large-size particles. Oceanic flights present less variability in the collected altitude and situations. The evolution of the PSD as a function of location into the MCS is more difficult to study due to the lack of organisation of the oceanic MCSs, as may be observed in Figure 2(b) and (c). Sherwood *et al.* (2006) mention a generally higher concentration of small-size crystals in the upper part of the continental MCS with respect to oceanic systems. They relate this observation to higher lightning occurrence in continental MCSs. They propose different explanations related to the intensity of the updraughts within continental MCSs. In such circumstances a greater number of aerosols can be activated as ice nuclei and then enhance homogeneous freezing. Another explanation is the ability of the liquid water to ascend higher in the cloud, because

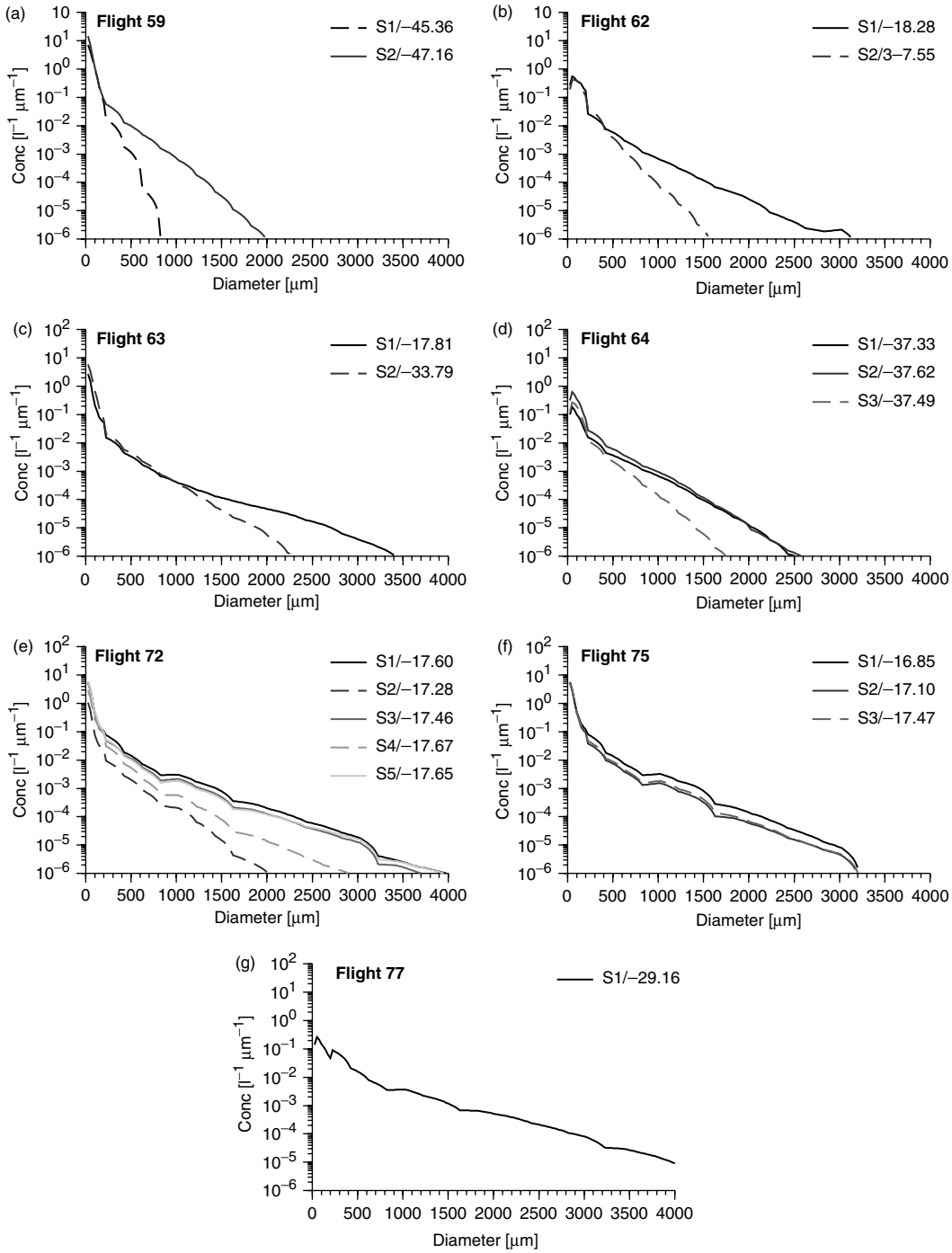

Figure 7. Mean PSD in l^{-1} μm^{-1} as a function of diameter in µm for all the segments of the AMMA experiment (one level of grey per flight segment with the associated temperature in °C) with one panel per flight: (a) flight 59, (b) flight 62, (c) flight 63, (d) flight 64, (e) flight 72, (f) flight 75 and (g) flight 77. Solid/dashed lines are for stratiform/cirriform segments.

of aerosol suppression of the warm-rain process and/or increasing ice splinters (Sherwood *et al.*, 2006).

4.2. Normalised particle size distribution

Testud *et al.* (2001) proposed a formalism that allows comparison of very different drop size distributions (DSDs) in the liquid part of precipitating systems. Delanoë *et al.* (2005) extended the same formalism to the ice phase. In their paper, they selected a unique mass–density relationship for all the datasets. The normalisation process of Testud *et al.* (2001) consists of scaling the diameter and concentration axes in such a way that the DSDs are independent of water content and mean volume-weighted diameter (D_m). They show that within tropical rain, the normalised DSD or shape function is fairly stable and that the intercept parameter has a distinct behaviour between convective and stratiform rains.

The extension of the Testud *et al.* (2001) normalisation process to the ice phase by Delanoë *et al.* (2005) allows

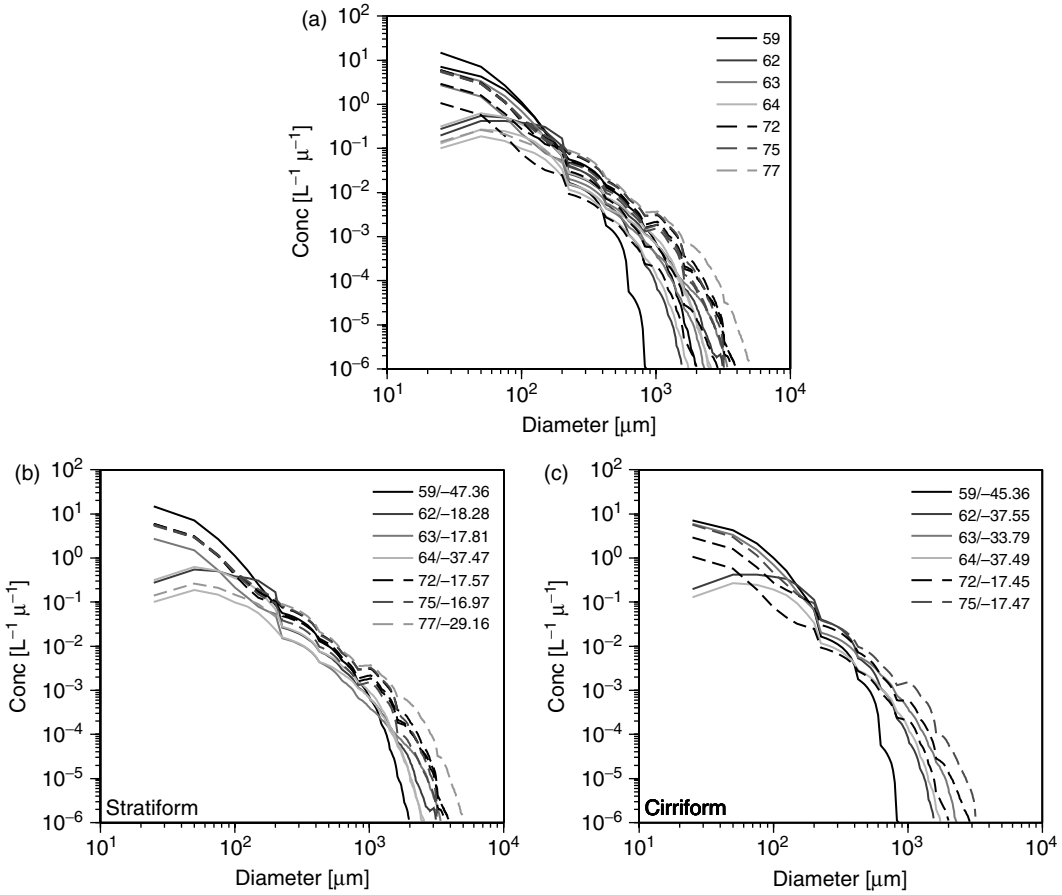

Figure 8. Mean PSD in l^{-1} µm^{-1} as a function of diameter in µm for all the segments of the AMMA experiment with solid lines for flights in the Niamey region and dashed lines for flights in the Dakar region. (a) All segments, (b) stratiform segments, (c) flights in cirriform segments. Each grey level corresponds to a different flight and the corresponding temperature in°C is shown in panels (b) and (c).

the PSD to be written as:

$$N(D_{\rm eq}) = N_0{}^* \; F(D_{\rm eq}/D_{\rm m}) \qquad (2)$$

where $N_0^* = \frac{4^4}{\pi\rho_{\rm water}} \frac{IWC}{D_{\rm m}^4}$ expressed in m^{-4}, $D_{\rm m} = \frac{\int N(D_{\rm eq}) D_{\rm eq}^4 \, {\rm d}D_{\rm eq}}{\int N(D_{\rm eq}) D_{\rm eq}^3 \, {\rm d}D_{\rm eq}}$ expressed in m, and F will be named in the following the shape function. $\rho_{\rm water}$ (10^6 g m^{-3}) is the density of water, IWC expressed in g m^{-3} is the ice water content (defined as $IWC = \frac{\pi\rho_{\rm water}}{6} \int N(D_{\rm eq}) D_{\rm eq}^3 \, {\rm d}D_{\rm eq}$) and $D_{\rm eq}$ is the equivalent melted diameter.

Mean normalised PSD shape (i.e. $N(D_{\rm eq}/D_{\rm m})/N_0{}^*$) as a function of $D_{\rm eq}/D_{\rm m}$ is shown for each segment of each flight in Figure 9. In the present study the density law from Brown and Francis (1995), which was used systematically in Delanoë *et al.* (2005), is replaced by the density law diagnosed in the previous section for each flight segment. It appears that the shape is rather invariant from one segment to another (except for Flight 59, Figure 9(a)) between normalised diameters ranging from 0.5 to 2, which correspond to the diameters with the largest amount of data. In contrast, the tail of the distribution shows a higher variability, which could also be due to a lower amount of data within this part of the PSD. The results obtained with the AMMA dataset are similar to the 'tropical' dataset of Delanoë *et al.* (2005) mainly coming from the CRYSTAL-FACE and CEPEX (Central Equatorial Pacific Experiment), their 'midlatitude' dataset consisting mainly of frontal systems. The same invariance as in this study of the normalised PSD shape is observed between 0.5 and 2, as well as the lack of a 'bump' in the vicinity of $D_{\rm eq}/D_{\rm m} = 1$, which was found to be a unique feature of the midlatitude normalised PSDs in Delanoë *et al.* (2005), as compared to the tropical PSDs. Wider distribution in the Tropics with respect to midlatitudes are attributed in Delanoë *et al.* (2005) to the growth process of ice particles in the Tropics (i.e. intense mesoscale convection) that leads to a wider distribution of particle diameters around the volume-weighted diameter.

Interestingly, it appears that the shape functions for a given flight are similar for all segments regardless of nature (stratiform or cirriform as in Flight 72 or 64, Figure 9(d) and (f) respectively) where rather strong differences were observable in Figure 7 or in temperature as in Flight 62 (Figure 9(b)). Both shape functions aligned nearly perfectly for $D_{\rm eq}/D_{\rm m}$ values larger than 0.5. These figures suggest that the expression of the PSD using the Testud *et al.* (2001) normalisation, generalised to the ice phase, would be useful for developing model parametrizations of the tropical ice clouds in the Tropics. As observed

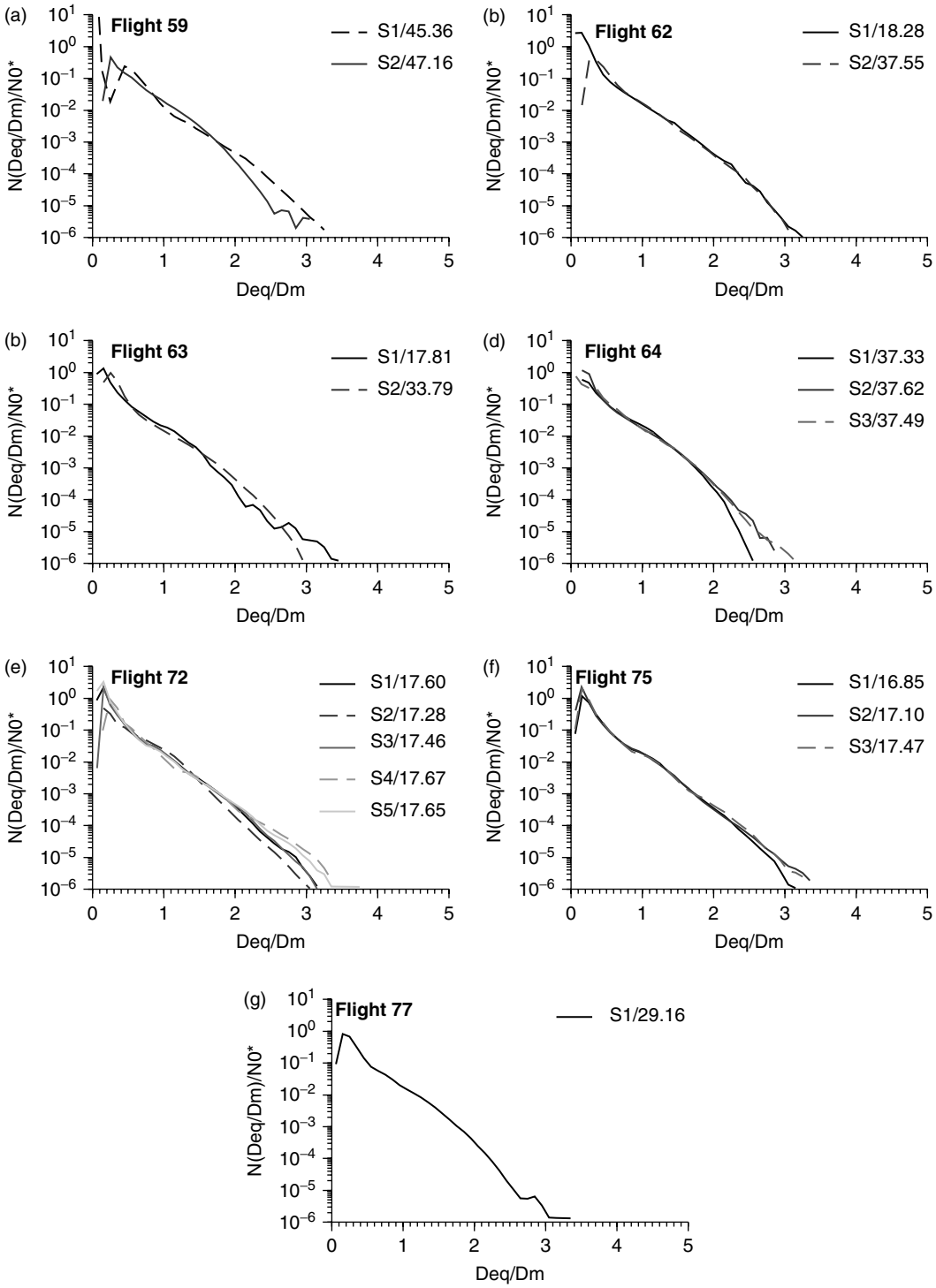

Figure 9. Mean shape function as a function of D_{eq}/D_m for all the segments of the AMMA experiment (one grey level per flight segment with the associated temperature in°C) with one panel per flight: (a) flight 59, (b) flight 62, (c) flight 63, (d) flight 64, (e) flight 72, (f) flight 75, and (g) flight 77. Solid/dashed lines are for stratiform/cirriform segments.

in rain events, the same shape may be used for different regions of the simulated systems. There would be no need to assume different PSD shapes depending of the particles encountered in the various regions of the system if this normalized PSD approach was implemented. It would also be very interesting to extend this normalisation process to a larger dataset of microphysical measurements, in particular to the NAMMA dataset (Zipser *et al.*, 2009), which was collected during the same period (15 August–15 September 2006) further west over the Atlantic.

One step further in the analysis of the shape function consists in comparing the shapes from one flight to another (top panel of Figure 10(a)) or between the different segment types (Figure 10(b) and (c)). As observed for the individual flights, all the PSDs exhibit the same

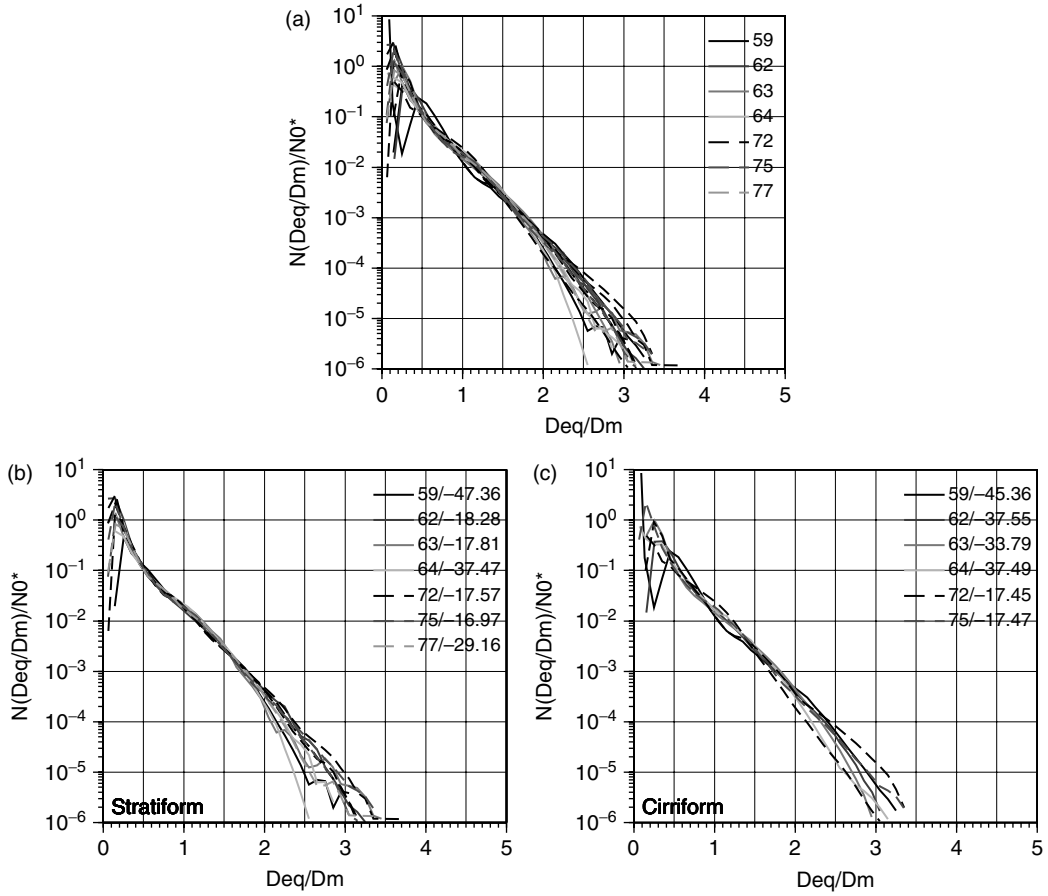

Figure 10. Mean shape function as a function of D_{eq}/D_m for all the segments of the AMMA experiment with solid lines for flights in the Niamey region and dashed lines for flights in the Dakar region. (a) All segments, (b) stratiform segments, (c) flights in cirriform segments. Each grey level corresponds to a different flight and the corresponding temperature in°C is shown in panels (b) and (c).

characteristics with an invariant shape for all flights between 0.5 and 2 and nearly linear behaviour in Figure 10(a), which correspond on these plots to an exponential shape. The variability increases below 0.5 and above 2. If one now compares the behaviour between stratiform and cirriform profiles (Figure 10(b) and (c)), it appears that the cirriform profiles are characterized by a smaller variability for D_{eq}/D_m larger than 2.

This section was dedicated to the study of the PSD in West African ice anvils, with and without normalisation. Differences were evidenced between stratiform and cirriform flight segments as well as between continental and coastal flight segments suggesting different growth processes or different efficiencies of growth processes in the different regions. Once the PSD is normalised, the resulting shape function is rather invariant for D_{eq}/D_m lower than 2 and greater than 0.5 and appears to be well approximated by an exponential shape (in agreement with the tropical results of Delanoë *et al.* (2005)).

5. Microphysical and Radiative Properties of West African MCSs

The AMMA experiment is the first campaign where microphysical measurements in African MCS anvils (in particular continental) are available. The purpose of this section is to provide the 'typical' microphysical and radiative parameter values that are encountered within such systems. The characterization of particle habits, associated density laws, and studies on particle shape variability carried out in the previous sections are of particular importance to reduce the errors associated with the calculation of these parameters from the PSDs. This can be seen in the following equations defining the effective radius (R_e, Eq. (3)), the reflectivity-weighted fall velocity (V_t, Eq. (4)), the IWC being defined in section 4.2:

$$R_e = \frac{10^6}{2}\frac{\int N(D_{eq})D_{eq}^3\ \mathrm{d}D_{eq}}{\int N(D_{eq})D_{eq}^2\ \mathrm{d}D_{eq}}, \tag{3}$$

$$V_t = \frac{\int v(D)\sigma_{bsc}(\rho, D, \lambda)F(D/D_m)\mathrm{d}D}{\int \sigma_{bsc}(\rho, D, \lambda)F(D/D_m)\ \mathrm{d}D}. \tag{4}$$

Heymsfield (2003b) examined the effect of sub-50 μm particles on IWC and total concentration (N_t, defined as the first moment of the PSD) and found that for all but the very uppermost part of the cloud layer (300 m depth), almost all of the IWC was contained in sizes measured by the imaging probes (i.e. larger than 100 μm). Within the AMMA experiment the only flight that took place at very low temperatures was Flight 59 (about −45°C). Therefore larger errors (underestimation of IWC) on the

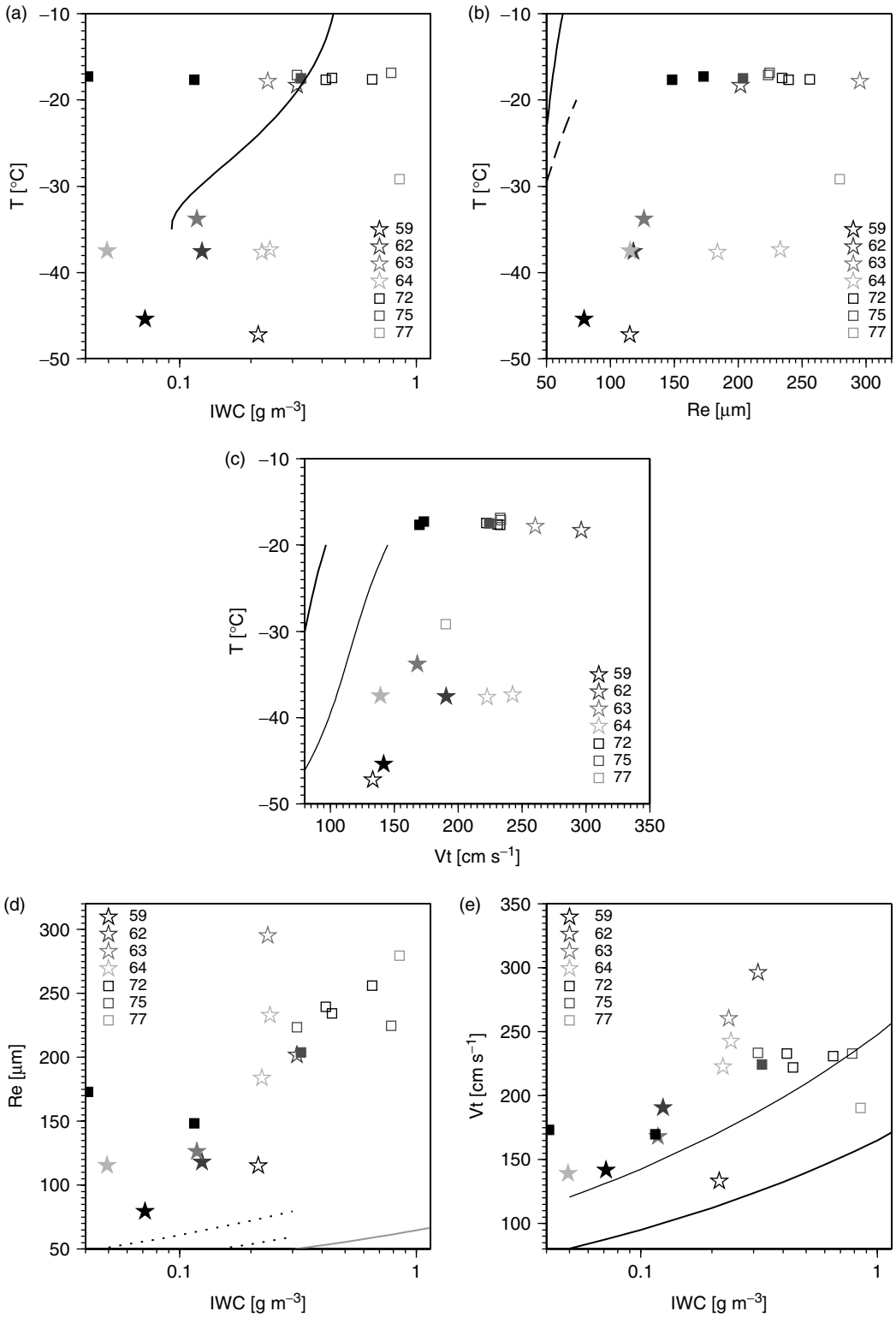

Figure 11. Observed microphysical and radiative parameters for the segments of all flights of the AMMA experiment. (a) Temperature stratification of IWC. (b) Temperature stratification of R_e. (c) Temperature stratification of V_t. (d) R_e as a function of IWC (e) V_t as a function of IWC. Each colour corresponds to a different flight with stars for the continental flights and squares for the oceanic and coastal flights. Filled symbols are for cirriform segments. Superimposed on the various panels are some corresponding statistical relationships found in the literature: Solid black lines are for Heymsfield (2003b), dashed black line for Ou and Liou (1995), dotted black lines for Sun and Rikus (1999), and solid grey line for Lohmann and Roeckner (1996).

estimates of the microphysical and radiative parameters are expected for this flight.

Generally, in models, the interaction of radiation with ice cloud is incorporated through the parametrization of single scattering properties in terms of effective radius R_e. Although it can be defined without ambiguity for liquid water clouds, there are lots of definitions of R_e for ice clouds in these parametrizations, owing to the underlying assumptions in the radiation code about the non-sphericity of ice crystals and their optical properties (see McFarquhar and Heymsfield, 1998). The definition by Stephens *et al.* (1990) (Eq. (3)) has been chosen in this paper because it is expressed in term of D_{eq}. At this step it must also be recalled that the small particles (smaller that 100 μm) are not included in the PSDs. As a result, R_e derived from this study may be overestimated.

Figure 11(a), (b) and (c) show the stratification of these parameters as a function of temperature. The general trend of these parameters is, as expected from previous studies of tropical cloud systems (Heymsfield and McFarquhar, 1996 or McFarquhar and Heymsfield, 1996; Heymsfield *et al.*, 2002; Heymsfield, 2003a, for instance), to increase with temperature, with a large variability for a given temperature.

Temperature ranges between −15 and −50°C in the present study. In particular for IWC (Figure 11(a)) it appears that cirriform profiles (filled symbols) are characterised by the lowest values of IWC. They also correspond to segments furthest from the convective cores (according to the conceptual scheme proposed by Houze and Betts (1981) where the convective core is followed by a stratiform region and then a cirriform anvil), suggesting that a part of the IWC present in the anvil is originating from the convective core as suggesting by Cetrone and Houze (2009). The same behaviours are also observed for the other parameters: lower R_e and V_t in cirriform segments compared to stratiform ones. The segments where the density law corresponds to less dense hydrometeors is also associated with lower terminal fall speeds.

The coastal and oceanic profiles are for most of them collected at the same temperature (−17°C). It is therefore difficult to interpret their stratification with temperature. It is noted that at this temperature the values of IWC span more than one order of magnitude. For the continental flights, a larger range of temperature was sampled within the various flights. It is found for the stratiform segments, in agreement with Griffith *et al.* (1980) who analysed data collected primarily in anvils and dissipating thick stratiform precipitation regions, that the magnitude of IWCs are mostly from 0.1 to 0.5 g m^{-3} and change by only a factor of two or three with height.

A second purpose of this section is to highlight the ability of some commonly used microphysical or radiative model parametrizations in reproducing the observed values in African MCSs. It must be noted that most mesoscale models now hold very sophisticated ice microphysics schemes and use several ice hydrometeor species. The problem may be different for general circulation models (GCMs) or radiative parametrizations. In such circumstances it is not directly a particle habit that is assumed but statistical relationships that link the microphysical or radiative parameters to the state variables of the model (for instance temperature). More sophisticated GCMs provide prognostic schemes for microphysics for instance but it remains necessary to evaluate whether or not such models are able to reproduce the observed values and are therefore able to correctly take into account the feedbacks associated with the MCS ice anvils.

Some statistical relationships (Ou and Liou, 1995; Sun and Rikus, 1999; Heymsfield, 2003b), fitted to observational datasets, the two first ones being used for instance in the radiative scheme of the French mesoscale model MESO-NH (Lafore *et al.*, 1998), have been superimposed in Figure 11.

Heymsfield (2003b) (solid black line in Figure 11(a)) proposed a relationship that captures the tendency of IWC to increase with temperature. It is observed (and it was also noted in this study) that the spread of IWC is large but his fitted law represents rather well the observed value in the West African anvils. Following the same idea, the stratification of R_e with temperature is compared to the statistical relationships proposed by Heymsfield (2003b) and Ou and Liou (1995) (solid black line and dashed black line respectively in Figure 11(b)). This comparison must be undertaken carefully, since several definitions of R_e may be found in the literature as noted by McFarquhar and Heymsfield (1998) in their review paper. For instance, Heymsfield (2003b) makes comparison of the Fu (1996) and Mitchell (2002) definitions for the same particle habit and shows the R_e values computed from the definition of Mitchell (2002) are 30% larger than those computed from the definition of Fu (1996). Moreover, the various laws, even if they generally use these definitions, are not all computed using the same assumption on particle habit and therefore are not directly comparable. Another point is the range of diameter considered in order to build these relationships: 50 μm to 1 cm for Heymsfield (2003b) (2D-C and HVPS data), 20 to 200 μm (1D-C and 1D-P data) for Ou and Liou (1995), 5 μm to 1 mm (VISP and 2D-C) for Sun and Rikus (1999) since, as stressed by Zender and Kiehl (1994), the omission of small-size particles leads to an overestimation of the size parameter. Heymsfield (2003b) estimates that the effective diameter computed in his paper may be overestimated by about 20% near cloud top and by a lesser amount deeper into the cloud layers. The small diameters are not considered in the present study leading to overestimated R_e but it must be noted that it is the case of virtually all *in situ* microphysical studies so far, as recalled in section 2 (Heymsfield, 2003b, for instance). Such laws are also derived using a very limited dataset like tropical or midlatitude cirrus measurements for instance. However a given law is generally used in models indifferently at all geographic locations. These reasons explained why R_e values derived from these relationships are shown as they are (no re-scaling depending for instance on the particle habit has been attempted) in Figure 11(b) and superimposed on the effective radius computed using the definition of Stephens

et al. (1990). The idea is mainly to provide an order-of-magnitude estimate and more work will be needed in the near future to compare our measurements to previous results, results from the Niamey ARM Mobile Facility (Protat *et al.*, 2009), and estimates from the RASTA radar observations, which will be the focus of future research. In particular the mean cross-sectional area of the observed particles is needed. It appears from the comparison displayed in Figure 11(b) that the measured R_e values are about twice as large as those obtained from the statistical relationships with large differences between Ou and Liou (1995) and Heymsfield (2003b) also. The same kind of comparison is also undertaken for the terminal fall speed and the Heymsfield (2003b) relationship (black line in Figure 11(d)). It is often the mass-weighted fall speed that is parametrized. Matrosov and Heymsfield (2000) compare the mass-weighted and reflectivity-weighted fall velocities and show that the ratio of the reflectivity-weighted to mass-weighted fall speed generally ranges between 1.2 and 2, and recommend a value of 1.5. The thin black line corresponds to this 'corrected' reflectivity-weighted fall speed and despite this correction, the Heymsfield (2003b) fall velocities are found to be smaller than the fall speeds estimated in the present study.

A second family of statistical relationships makes use of the IWC in order to derive R_e or V_t in models. Comparisons for R_e are proposed in Figure 11(d) with Sun and Rikus (1999) (dotted line, that also includes a temperature dependency) and with Lohmann and Roeckner (1996) (solid grey line). As for the parametrization with temperature, it appears that the computed R_e are more than a factor 2 smaller than the estimated values from the present study. Figure 11(e) shows the comparison of fall speeds (corrected reflectivity-weighted in thin black line and mass-weighted in black line) from the Heymsfield (2003b) relationship. Even if a systematic bias is observed the (corrected) velocities tend to be rather good 'proxies' of the V_t–IWC relationship for oceanic segments. For continental flights, the reflectivity-weighted fall velocities increase more rapidly with IWC compared to those derived from the corrected Heymsfield (2003b) relationship.

6. Conclusions

Insights into the particle habits, the characteristics of the particle size distributions and microphysical and radiative properties of tropical ice anvils and cirriform clouds observed during the AMMA campaign have been described in this paper. It has to be remembered that before the AMMA experiment, no *in situ* measurements existed of continental African MCS ice anvils. Despite some measurement limitations detailed in section 2, this dataset is therefore of particular importance.

A major goal of this paper was to infer the more representative density–size relationship and the growth processes involved within such ice clouds within various regions of the MCSs anvils (edge or non-precipitating 'cirriform' segments and more active or precipitating 'stratiform' regions). 2D-C images show a rather small variability of encountered particles within rimed aggregates observed whatever the sampled region or altitude considered. In agreement with this result, the retrieved density–size relationships for the various segments have been found close to relationships for rimed particles proposed by Locatelli and Hobbs (1974) (see Figure 5(a)). This diagnostic has been indirectly validated by looking at the roughness exponent and 2D-C images. There is a relatively low scatter in the roughness exponent values, but relatively larger values (indicating a growth by aggregation) in the cirriform segments, while lower values (corresponding to more rimed particles) are found in stratiform segments even at relatively high altitudes. According to Houze (1997) it is likely that upward vertical motions in stratiform regions are too weak to uplift high concentrations of cloud liquid water in order to form rimed particles within the anvil. Yuter and Houze (1995) suggested that the moderately sized particles formed in the convective cells are spread by the expanding buoyant parcels over a wider area, and they form the raw material of the stratiform cloud deck that becomes thick and persistent in the MCS. They stated that the growth of glaciated precipitation particles that were rising in the storm was occurring in the range 2 to 5 m s^{-1}. At these moderate vertical velocities, sufficient vapour and liquid water are available for depositional and/or accretional growth. Differential reflectivity observations in this Florida MCS suggest graupel. Vertical motions in continental West African MCSs can locally reach higher vertical velocity (see for instance Zipser, 1994) and are then more likely to produce larger rimed particles. The advection of rimed particles from the deep convection core toward the anvils may rather explain the presence of rimed particles in stratiform segments, as proposed by Cetrone and Houze (2009) or Heymsfield *et al.* (2002).

As stated in Houze (1997), if high-resolution numerical prediction models are to forecast accurately the location, amount and type of precipitation, they must represent (either explicitly or by using parametrizations) the microphysical growth processes accurately. This determination has also great importance if one wants to make use of spaceborne microwave radiometer observations over the continent to derive rainfall rates produced by these MCSs since for such instrumentation only the high-frequency channels (sensitive to ice) can be used (the lower-frequency channel being saturated by the ground emissivity), and particle habits have to be assumed. The insights on particle habit obtained in this paper contribute to better constrain these algorithms.

Differences in the PSD characteristics between stratiform and cirriform segments and between continental and coastal segments have been investigated. All sampled MCSs were well characterized by exponential shape distributions for particle diameters larger than 500 μm for continental systems or 800 μm for coastal and oceanic systems respectively. The decrease of concentration with size is found more rapid for cirriform segments than in stratiform regions. A large amount of small-diameter

particles is also found for the colder continental cirriform segments. A normalisation has been applied to the observed PSD following Delanoë *et al.* (2005). The resulting shape function is found to be virtually invariant for values of D_{eq}/D_m lower than 2 and greater than 0.5. Between these limits, the shape appears exponential. These results may be extended to larger normalised diameter for the cirriform segments where the scatter is smaller. However it appears that the shape is rather similar for both types of profiles suggesting that it would be interesting to parametrize the processes acting in the anvil using the Testud *et al.* (2001)/Delanoë *et al.* (2005) formalism and approximated normalised PSD shapes since the microphysical variability would then be fully included in the $N_0{}^*$ and D_m parameters.

The microphysical and radiative properties of West African anvils have been estimated for all the flights and sorted according to the segment type, the altitude, and their location with respect to the convective cores. Expected trends obtained in previous tropical anvils are found with the IWC, R_e and V_t increasing from cloud top to cloud base. These results have been obtained from a composite of several constant altitude segments (ensuring that temperature is close to constant and that several cloud systems or cloud regions are not mixed). Although incomplete, this dataset may be used as support for evaluating the ability of a given parametrization to realistically represent the ice anvils and the associated feedbacks within models. This aspect has been illustrated for several relationships and it is found that the proposed laws in the literature (Heymsfield, 2003b; Ou and Liou, 1995; Sun and Rikus, 1999 or Lohmann and Roeckner, 1996) are not able to provide R_e and V_t as large as observed. The Heymsfield (2003b) relationships show the best agreement for IWC parametrized as a function of temperature and of V_t parametrized as a function of IWC, suggesting that these relationships are suitable for simulating African MCS anvils.

More generally, a primary objective of our studies using the AMMA dataset was initially to study in detail the evolution of a given MCS anvil in order to better understand the processes acting at the various stages of the life cycle at the different altitudes and the relationship that exists between the anvil microphysics and the leading deep convection. Due to the strong limitation of the present dataset it appears necessary for such a study to use a mesoscale model implementing a detailed microphysical parametrization. This is the work proposed by Penide *et al.* (2010, this issue). An important step for this purpose is to ensure that the microphysical or radiative schemes are able to reproduce the observed values. The present study contributes to such an evaluation, as shown in Penide *et al.* (2010, this issue).

A generalisation of these results is also of major interest since, as stressed in this paper, the data in this region are very sparse. Since 2006 the CloudSat–CALIPSO tandem has provided continuous measurements of cloud properties, in particular of ice clouds, and passes at least twice a day over this African region. By making use of clustering techniques, the climatology of ice anvil microphysical and radiative properties may be constructed within the different regions of the anvil, for different convective intensity within different life stages (emerging, mature or decaying for instance) over land or ocean and with consideration of the diurnal cycle. The present results may be used as a reference for evaluating the spaceborne retrievals of microphysical and radiative parameters.

The results enclosed in this paper let us think that additional flights with additional microphysical measurements, in particular of small crystals (size and concentration) and liquid water content would be of great interest to go further in the diagnostics presented in this paper. It would also be very interesting to extend the documentation to the aerosol properties. In this region desert dust can serve as ice-forming nuclei and thus may alter the cloud microphysical structure. Van den Heever *et al.* (2006) examined the full range of convective cloud microphysical and dynamics sensitivities to ice nuclei within mesoscale model simulations of a CRYSTAL-FACE case. Enhanced ice nuclei concentrations resulted in more ice mass (less liquid and vapour mass) passing into the anvil and a deeper anvil. Such factors in turn influence the radiative forcing properties of anvils and differences may be sought with respect to oceanic or continental location due to differences in atmospheric composition.

Acknowledgements

The authors are grateful to Thomas Fiolleau and Rémy Roca from the Laboratoire de Météorologie dynamique (CNRS) for providing the results of the tracking algorithm and for useful discussions on their use. We really appreciate the help of Fatima Karbou and Elisabeth Gérard for access to the microwave measurements and we would like to thank E.J. Zipser (and his students), E.R. Williams and an anonymous reviewer for their very helpful comments.

The TMI data were provided by the TRMM Science Data and Information System (TSDIS) at NASA GSFC. SSM/I data were provided by the Global Hydrology Resource Center (GHRC) at the Global Hydrology and Climate Center, Huntsville, Alabama. The AMSRE data were obtained through the National Snow and Ice Data Center (NSDIC).

Based on a French initiative, AMMA was built by an international scientific group and is currently funded by a large number of agencies, especially from France, United Kingdom, USA and Africa. It has been the beneficiary of a major financial contribution from the European Community's Sixth Framework Research Programme. Detailed information on scientific coordination and funding is available on the AMMA International web site http://www.amma-international.org. The second author received funding from NERC grant NE/C519697/1. This work has also been strongly supported by the French Space Agency (CNES) through the funding of the RASTA instrument and of a significant portion of the flight hours during AMMA.

References

Ackerman TP, Liou K-N, Valero FPJ, Pfister L. 1988. Heating rates in tropical anvils. *J. Atmos. Sci.* **45**: 1606–1623.

Arnaud Y, Desbois M, Maizi J. 1992. Automatic tracking and characterization of African convective systems on Meteosat pictures. *J. Appl. Meteorol.* **31**: 443–453.

Bouniol D, Protat A, Plana-Fattori A, Giraud M, Vinson J-P, Grand N. 2008. Comparison of airborne and spaceborne 95-GHz radar reflectivities and evaluation of multiple scattering effects in spaceborne measurements. *J. Atmos. Oceanic Technol.* **25**: 1983–1995.

Brown PRA, Francis PN. 1995. Improved measurements of the ice water content in cirrus using a total-water probe. *J. Atmos. Oceanic Technol.* **12**: 410–414.

Caniaux G, Redelsperger J-L, Lafore J-P. 1994. A numerical study of the stratiform region of a fast-moving squall line. Part I: General description and water and heat budgets. *J. Atmos. Sci.* **51**: 2046–2074.

Cecil DJ, Goodman SJ, Boccippio DJ, Zipser EJ, Nesbitt SW. 2005. Three years of TRMM precipitation features. Part I: Radar, radiometric, and lightning characteristics. *Mon. Weather Rev.* **133**: 543–566.

Cetrone J, Houze Jr RA. 2009. Anvil clouds of tropical mesoscale convective systems in monsoon regions. *Q. J. R. Meteorol. Soc.* **135**: 305–317.

Delanoë J, Protat A, Testud J, Bouniol D, Heymsfield AJ, Bansemer A, Brown PRA, Forbes RM. 2005. Statistical properties of the normalized ice particle size distribution. *J. Geophys. Res.* **110**: D10201, DOI:10.1029/2004JD005405.

Deng M, Mace GG. 2008. Cirrus cloud microphysical properties and air motion statistics using cloud radar Doppler moments: Water content, particle size, and sedimentation relationships. *Geophys. Res. Lett.* **35**: L17808, DOI:10.1029/2008GL035054.

Donovan DP, Quante M, Schlimme I, Macke A. 2004. Use of equivalent spheres to model the relation between radar reflectivity and optical extinction of ice cloud particles. *Appl. Opt.* **43**: 4929–4990.

Duroure C, Larsen HR, Isaka H, Personne P. 1994. 2D image population analysis. *Atmos. Res.* **34**: 195–205.

Field PR, Heymsfield AJ. 2003. Aggregation and scaling of ice crystal size distributions. *J. Atmos. Sci.* **60**: 544–560.

Field PR, Heymsfield AJ, Bansemer A. 2006. Shattering and particle interarrival times measured by optical array probes in ice clouds. *J. Atmos. Oceanic Technol.* **23**: 1357–1371.

Fiolleau T, Tomasini M, Roca R, Lafore J-P, Laurent H, Lebel T, Ramage K. 2009. Summertime climatology of mesoscale convective systems over West Africa from 24-years of Meteosat observations. *Geophys. Res. Abstracts* **11**: EGU2009–9104.

Francis PN, Hignett P, Macke A. 1998. The retrieval of cirrus cloud properties from aircraft multi-spectral reflectance measurements during EUCREX'93. *Q. J. R. Meteorol. Soc.* **124**: 1273–1291.

Fu Q. 1996. An accurate parameterization of the solar radiative properties of cirrus clouds for climate models. *J. Climate* **9**: 2058–2082.

Griffith KT, Cox SK, Knollenberg RG. 1980. Infrared radiative properties of tropical cirrus clouds inferred from aircraft measurements. *J. Atmos. Sci.* **37**: 1077–1087.

Heymsfield AJ. 1972. Ice crystal terminal velocities. *J. Atmos. Sci.* **29**: 1348–1357.

Heymsfield AJ. 2003a. Properties of tropical and midlatitude ice cloud particle ensembles. Part I: Median mass diameters and terminal velocities. *J. Atmos. Sci.* **60**: 2573–2591.

Heymsfield AJ. 2003b. Properties of tropical and midlatitude ice cloud particle ensembles. Part II: Applications for mesoscale and climate models. *J. Atmos. Sci.* **60**: 2592–2611.

Heymsfield AJ, Kajikawa M. 1987. An improved approach to calculating terminal velocities of plate-like crystals and graupel. *J. Atmos. Sci.* **44**: 1088–1099.

Heymsfield AJ, McFarquhar GM. 1996. High albedos of cirrus in the tropical Pacific warm pool: Microphyiscal interpretations from CEPEX and from Kwajalein, Marshall Islands. *J. Atmos. Sci.* **53**: 2424–2451.

Heymsfield AJ, Parrish JL. 1986. An interactive system for processing PMS two-dimensional imaging probe data. *J. Atmos. Oceanic Technol.* **3**: 734–736.

Heymsfield AJ, Bansemer A, Field PR, Durden SL, Stith JL, Dye JE, Hall W, Grainger CA. 2002. Observations and parameterizations of particle size distributions in deep tropical cirrus and stratiform precipitating clouds: Results from *in situ* observations in TRMM field campaigns. *J. Atmos. Sci.* **59**: 3457–3491.

Heymsfield AJ, Bansemer A, Schmitt C, Twohy C, Poellot MR. 2004. Effective ice particle densities derived from aircraft data. *J. Atmos. Sci.* **61**: 982–1003.

Heymsfield AJ, Bansemer A, Twohy CH. 2007. Refinements to ice particle mass dimensional and terminal velocity relationships for ice clouds. Part I: Temperature dependence. *J. Atmos. Sci.* **64**: 1047–1067.

Houze Jr RA. 1977. Structure and dynamics of a tropical squall-line system. *Mon. Weather Rev.* **105**: 1540–1567.

Houze Jr RA. 1982. Cloud clusters and large-scale vertical motions in the Tropics. *J. Meteorol. Soc. Jpn* **60**: 396–410.

Houze Jr RA. 1989. Observed structure of mesoscale convective systems and implications for large-scale heating. *Q. J. R. Meteorol. Soc.* **115**: 425–461.

Houze Jr RA. 1997. Stratiform precipitation in regions of convection: A meteorological paradox? *Bull. Am. Meteorol. Soc.* **78**: 2197–2196.

Houze Jr RA. Betts AK. 1981. Convection in GATE. *Rev. Geophys.* **19**: 541–576.

Korolev A, Isaac GA. 2005. Shattering during sampling by OAPs and HVPS. Part I: Snow particles. *J. Atmos. Oceanic Technol.* **22**: 528–542.

Lafore J-P, Stein J, Asencio N, Bougeault P, Ducrocq V, Duron J, Fischer C, Héreil P, Mascart P, Masson V, Pinty J-P, Redelsperger J-L, Richard E, Vilà-Guerau de Arellano J. 1998. The Meso-NH Atmospheric Simulation System. Part I: Adiabatic formulation and control simulations. *Ann. Geophys.* **16**: 90–109.

Leary CA, Houze Jr RA. 1980. The contribution of mesoscale motions to the mass and heat fluxes of an intense tropical convective system. *J. Atmos. Sci.* **37**: 784–796.

Li L, Heymsfield GM, Tian L, Racette PE. 2005. Measurements of ocean surface backscattering using an airborne 94-GHz cloud radar: Implication for calibration of airborne and spaceborne W-band radars. *J. Atmos. Oceanic Technol.* **22**: 1033–1045.

Locatelli JD, Hobbs PV. 1974. Fall speeds and masses of solid precipitation particles. *J. Geophys. Res.* **79**: 2185–2197.

Lohmann U, Roeckner E. 1996. Design and performance of a new cloud microphysics scheme developed for the ECHAM general circulation model. *Clim. Dyn.* **12**: 557–572.

Mace GG, Deng M, Soden B, Zipser EJ. 2006. Association of tropical cirrus in the 10–15-km layer with deep convective sources: An observational study combining millimeter radar data and satellite-derived trajectories. *J. Atmos. Sci.* **63**: 480–503.

McFarquhar GM, Heymsfield AJ. 1996. Microphysical characteristics of three anvils sampled during the Central Equatorial Pacific Experiment. *J. Atmos. Sci.* **53**: 2401–2423.

McFarquhar GM, Heymsfield AJ. 1998. The definition and significance of effective radius for ice clouds. *J. Atmos. Sci.* **55**: 2039–2052.

McFarquhar GM, Um J, Freer M, Baumgardner D, Kok GL, Mace GG. 2007. Importance of small ice crystals to cirrus properties: Observations from the Tropical Warm Pool International Cloud Experiment (TWP-ICE). *Geophys. Res. Lett.* **34**: L13803, DOI:10.1029/2007GL029865.

Macklin WC. 1962. The density and structure of ice formed by accretion. *Q. J. R. Meteorol. Soc.* **88**: 30–50.

Mathon V, Laurent H. 2001. Life cycle of Sahelian mesoscale convective cloud systems. *Q. J. R. Meteorol. Soc.* **127**: 377–406.

Matrosov SY, Heymsfield AJ. 2000. Use of Doppler radar to assess ice cloud particle fall velocity-size relations for remote sensing and climate studies. *J. Geophys. Res.* **105**: 22427–22436.

Mitchell DL. 1996. Use of mass- and area-dimensional power laws for determining precipitation particle terminal velocities. *J. Atmos. Sci.* **53**: 1710–1723.

Mitchell DL. 2002. Effective diameter in radiation transfer: General definition, applications, and limitations. *J. Atmos. Sci.* **59**: 2330–2346.

Mohr KI, Zipser EJ. 1996. Defining mesoscale convective systems by their 85-GHz ice-scattering signatures. *Bull. Am. Meteorol. Soc.* **77**: 1179–1189.

Ou S-C, Liou K-N. 1995. Ice microphysics and climatic temperature feedback. *Atmos. Res.* **35**: 127–138.

Penide G, Giraud V, Bouniol D, Dubuisson P, Duroure C, Protat A, Cautenet S. 2010. Numerical simulation of the 7 to 9 September 2006 AMMA mesoscale convective system: Evaluation of the dynamics and cloud microphysics using synthetic observations. *Q. J. R. Meteorol. Soc.* **136**(s1): 305–323.

Protat A, Pelon J, Grand N, Delville P, Laborie P, Vinson J-P, Bouniol D, Bruneau D, Chepfer H, Delanoë J, Haeffelin M, Noël V, Tinel C. 2004. Le projet Rali: Combinaison d'un radar et d'un lidar pour l'étude des nuages faiblement précipitants. *La Météorologie* **47**: 23–33.

Protat A, Bouniol D, Delanoë J, May PT, Plana-Fattori A, Hasson A, O'Connor E, Görsdorf U, Heymsfield AJ. 2009. Assessment of CloudSat reflectivity measurements and ice cloud properties using ground-based and airborne cloud radar observations. *J. Atmos. Oceanic Technol.* **26**: 1717–1741.

Protat A, Delanoë J, Plana-Fattori A, May PT, O'Connor EJ. 2009. The statistical properties of tropical ice clouds generated by the West African and Australian monsoons, from ground-based radar–lidar observations. *Q. J. R. Meteorol. Soc.* **136**(s1): 346–364.

Pruppacher HR, Klett JD. 1978. *Microphysics of clouds and precipitation*. D. Reidel: Dordrecht.

Redelsperger J-L, Diedhiou A, Flamant C, Janicot S, Lafore J-P, Lebel T, Polcher J, Bourlès B, Caniaux G, de Rosnay P, Desbois M, Eymard L, Fontaine B, Geneau I, Ginoux K, Hoepffner M, Kane CSE, Law K, Mari C, Marticoréna B, Mougin E, Pelon J, Peugeot C, Protat A, Roux F, Sultan B, van den Akker E. 2006. AMMA, une étude multidisciplinaire de la mousson ouest-africaine. *La Météorologie* **54**: 22–32.

Rickenbach T, Kucera P, Gentry M, Carey L, Lare A, Lin R-F, Demoz B, Starr DO'C. 2008. The relationship between anvil clouds and convective cells: A case study in south Florida during CRYSTAL-FACE. *Mon. Weather Rev.* **136**: 3917–3932.

Sherwood SC. 1999. On moistening of the tropical troposphere by cirrus cloud. *J. Geophys. Res.* **104**: 11949–11960.

Sherwood SC, Phillips VTJ, Wettlaufer JS. 2006. Small ice crystals and the climatology of lightning. *Geophys. Res. Lett.* **33**: L05804, DOI:10.1029/2005GL025242.

Stephens GL, Tsay S-C, Stackhouse Jr PW, Flatau PJ. 1990. The relevance of the microphysical and radiative properties of cirrus clouds to climate and climatic feedback. *J. Atmos. Sci.* **47**: 1742–1754.

Stephens GL, Vane DG, Boain RJ, Mace GG, Sassen K, Wang Z, Illingworth AJ, O'Connor EJ, Rossow WB, Durden SL, Miller SD, Austin RT, Benedetti A, Mitrescu C, the CloudSat Science Team. 2002. The CloudSat mission and the A-Train: A new dimension of space-based observations of clouds and precipitation. *Bull. Am. Meteorol. Soc.* **83**: 1771–1790.

Stith JL, Haggerty JA, Heymsfield AJ, Grainger CA. 2004. Microphysical characteristics of tropical updrafts in clean conditions. *J. Appl. Meteorol.* **43**: 779–794.

Sun Z, Rikus L. 1999. Parametrization of effective sizes of cirrus-cloud particles and its verification against observations. *Q. J. R. Meteorol. Soc.* **125**: 3037–3055.

Testud J, Oury S, Black RA, Amayenc P, Dou X. 2001. The concept of 'normalized' distribution to describe raindrop spectra: A tool for cloud physics and cloud remote sensing. *J. Appl. Meteorol.* **40**: 1118–1140.

van den Heever SC, Carrió GG, Cotton WR, DeMott PJ, Prenni AJ. 2006. Impacts of nucleating aerosol on Florida storms. Part I: Mesoscale simulations. *J. Atmos. Sci.* **63**: 1752–1775.

Webster PJ, Stephens GL. 1980. Tropical upper-tropospheric extended clouds: Inferences from Winter MONEX. *J. Atmos. Sci.* **37**: 1521–1541.

Williams ER, Zhang R. 1996. Density of rime in laboratory simulations of thunderstorm microphysics and electrification. *J. Geophys. Res.* **101**: 29715–29719.

Yuter SE, Houze Jr RA. 1995. Three-dimensional kinematic and microphysical evolution of Florida cumulonimbus. Part II: Frequency distributions of vertical velocity, reflectivity and differential reflectivity. *Mon. Weather Rev.* **123**: 1941–1963.

Zender CS, Kiehl JT. 1994. Radiative sensitivities of tropical anvils to small ice crystals. *J. Geophys. Res.* **99**: 25869–25880.

Zikmunda J, Vali G. 1972. Fall patterns and fall velocities of rimed ice crystals. *J. Atmos. Sci.* **29**: 1334–1347.

Zipser EJ. 1994. Deep cumulonimbus cloud systems in the Tropics with and without lightning. *Mon. Weather Rev.* **122**: 1837–1851.

Zipser EJ, LeMone MA. 1980. Cumulonimbus vertical velocity events in GATE. Part II: Synthesis and model core structure. *J. Atmos. Sci.* **37**: 2458–2469.

Zipser EJ, Twohy CH, Tsay S-C, Thornhill KL, Tanelli S, Ross R, Krishnamurti TN, Ji Q, Jenkins G, Ismail S, Hsu NC, Hood R, Heymsfield GM, Heymsfield AJ, Halverson J, Goodman HM, Ferrare R, Dunion JP, Douglas M, Cifelli R, Chen G, Browell EV, Anderson B. 2009. The Saharan Air Layer and the fate of African easterly waves – NASA's AMMA field study of tropical cyclogenesis. *Bull. Am. Meteorol. Soc.* **90**: 1137–1156.